CONTROL AND CHARACTERIZATION OF A CYCLOTRON PROTON BEAM

A Thesis

presented to

the Faculty of the Graduate School

at the University of Missouri-Columbia

In Partial Fulfillment

of the Requirements for the Degree

Master of Science

by

MASLINA MOHD IBRAHIM

Dr. John Gahl, Thesis Supervisor

JULY 2010

The undersigned, appointed by the dean of the Graduate School, have examined the thesis entitled

CONTROL AND CHARACTERIZATION OF A CYCLOTRON PROTON BEAM

presented by Maslina Mohd Ibrahim,

a candidate for the degree of **Master of Science**

and hereby certify that, in their opinion, it is worthy of acceptance.

_____

Dr. Tina Smilkstein, Assistant Professor, Dept. of Electrical and Computer Engineering

_____

Dr. Naz Islam, Professor, Dept. of Electrical and Computer Engineering

_____

Dr. John Gahl, Professor, Dept. of Chemical Engineering

ACKNOWLEDGEMENTS

I would like to express my sincere appreciation to my advisor, Dr. John Gahl for his support and guidance with this thesis. His advice and kindness has been invaluable to me and it will be beneficial to my future work.

I am also grateful to Dr. Naz Islam and Dr. Tina Smilkstein for their valuable help and for serving as my thesis committee members.

I wish to express my thanks to Alex Saale, an engineer at cyclotron facility for his assistant and help in the research and system development. My gratitude also goes to Mike Klote, Brian Samuels, Richard Mcwhorter and Mike Harlow for their assistant that makes this thesis a success.

I am in deep gratitude to my best friends Yoon-Chee Pak and Yuritza Oliver who have always being optimistic, encouraged, supported and stayed beside me all the time during my graduate studies.

Special thanks to my family, my parents Mohd Ibrahim bin Uman and Azizah binti Hashim, my siblings for their love and patience.

I take this opportunity to thank the Government of Malaysia for their sponsor of my studies. Also to all my friends who stood by my side for their suggestions and friendship.

TABLE OF CONTENTS

ACKNOWLEDGEMENTS ii

LIST OF ILLUSTRATIONS vi

LIST OF TABLES ix

ABSTRACT x

CHAPTER

1. INTRODUCTION 1

    1.1 Introduction 1

        1.1.1 Charged Particle Beams 2

        1.1.2 Magnetic Force on Moving Charge 3

        1.1.3 Paraxial Beam Transport with Space Charge 4

        1.1.2 Magnetic Circuit Design 5

        1.1.2 Magnetic Properties of Material 7

    1.2 Research Goals and Intended Contributions 10

    1.3 Brief Description of Thesis Content 13

2. LITERATURE REVIEW 15

    2.1 Introduction 15

    2.2 Review of Control and Diagnostic of Proton Beams 16

    2.3 Magnetic Circuit and Finite Element Analysis 18

    2.4 Summary 20

3. CYCLOTRON 21
3.1 Introduction 21
3.2 PETtrace Cyclotron at MURR 23
3.3 Magnetic Safety Consideration 27

4. METHODOLOGY AND RESEARCH APPROACH.....29
4.1 Introduction 29
4.2 Cyclotron Proton Beam Parameters Analysis 31
4.2.1 Proton Particle Velocity.....32
4.2.2 Transverse Velocity 34
4.2.3 Transverse Distance.....35
4.3 Magnetic Circuit Design 38
4.4 Magnetic Finite Element Analysis 44
4.5 Implementation.....45
4.5.1 Experiment Set-up.....46
4.6 Diagnostic System.....51

5. FINITE ELEMENT METHOD MAGNETIC 54
5.1 Introduction 54
5.2 Model Construction and Design.....57
5.3 Boundary Condition 59
5.4 Simulation and Analysis on the Designed Magnetic Circuit 61
5.5 Analysis of Magnetic Circuit in the Magnetic Field Environment 67

6. RESULTS AND DISCUSSION 73

6.1 Introduction 73

6.2 Magnetic Circuit with Low Current in Field Free Space 74

6.3 Magnetic Circuit with High Current in Field Free Space 78

6.4 Deflection of the Cyclotron Beam 80

7. CONCLUSIONS AND FUTURE WORKS 86

7.1 Conclusions 86

7.2 Future works 87

REFERENCE 89

APPENDIX 93

LIST OF ILLUSTRATIONS

Figure **Page**

1.1 The right hand rule and the motion of a particle when the charge moves in an uniform magnetic field....3

1.2 (a) B-H curve of ferromagnetic materials (b) example of magnetic circuit 8

1.3 B-H curve of ANSI-1018 steel 9

1.4 The position of the cyclotron proton beam....11

1.5 The side view of cyclotron machine at MURR 11

3.1 Principles of a cyclotron. Cropped from U.S. Patent 1948384....21

3.2 The *dees* of the cyclotron at MURR 23

3.3 PETtrace radiotracer principle of operation....24

3.4 The 60.96 cm (24 inches) beam drift tube connected to the beam port of PETtrace cyclotron, MURR....26

3.5 Exploded view of the beam drift tube....26

3.6 Magnetic field of PETtrace cyclotron at MURR – top view 28

4.1 The schematic of the system....31

4.2 The schematic diagram of how the transverse velocity affected the path of the proton 36

4.3 Illustrations of the magnetic circuit using the right hand rule (a) the force is directed in the *y* direction (b) the force is directed in *x* direction. 38

4.4 The dimension of magnetic core....40

4.5 Effective (due to fringing) and actual cross section for the air gap....40

4.6 Equivalent circuit for analyzing the magnetic circuit 40

4.7 B-H curve for steel type ANSI-1018 43

4.8 Magnetic core with 50 turns of 10 AWG magnetic wires at each side 45

4.9 Magnetic field probe 46

4.10 The circuit for low current source testing 47

4.11 The stand for holding the magnetic circuit on the cyclotron machine 49

4.12 The magnetic circuit was placed at the beginning of the proton beam's drift tube (a) The whole view (b) Close up of the magnetic circuit 50

4.13 Schematic of Faraday cup (a) cross section for full exposure (b) cross section for partial exposure 52

4.14 Ceramic plate (a) full exposure (b) one section exposure 52

4.15 The placement of plate 3 to measure the position of the beam (a) top (b) right (c) left (d) bottom 53

4.16 The Faraday cup (a) ceramic plate 1 (b) ceramic plate 2 (c) ceramic plate 3 (d) Aluminum plate 53

5.1 Triangulation of Massachusetts 57

5.2 The 2-D geometry of the magnetic circuit regions 57

5.3 The meshed domain of the model 59

5.4 The simulation results at 100 Amps 62

5.5 The H-value profile for the magnetic core 64

5.6 The B-value profile for 1018 steel magnetic core 64

5.7 Magnetic field magnitude at the center of the gap with currents range from 0 to 350 Amps 65

5.8 Magnetic field magnitude at the center of the gap with currents range from 0 to 170 Amps 66

5.9 The deflection of the beams at different tube size 67

5.10 The simulation at 100 Amps where the force is in the y direction and the surrounding magnetic field is 0.005 T 68

5.11 The simulation at 100 Amps where the force is in the x direction and the surrounding magnetic field is 0.005T 69

5.12 A comparison of the magnetic field at the gap of the magnetic core between field free and cyclotron magnetic field environments with x and y deflection direction 69

5.13 The deflection result for the current range between 0 to 170 Amps for 15.24cm (6 inches) drift tube 70

5.14 The deflection result for the current range between 0 to 170 Amps for 20.32cm (8 inches) drift tube 71

5.15 The deflection result for the current range between 0 to 170 Amps for 60.96cm (24 inches) drift tube 71

6.1 Magnetic field magnitude for current range from 0 to 15 Amps 74

6.2 The location and orientation of data collected for low current experiment (a) vertical data (b) horizontal data 75

6.3 Magnitude of the flux density, |B| at the gap in the vertical direction (a) Simulation result from FEMM (b) Experimental result 76

6.4 Magnitude of the flux density, |B| at the gap in the horizontal direction (a) Simulation result from FEMM (b) Experimental result 77

6.5 The simulation result of 114 Amps, 80 Amps and 58 Amps currents when applied to the magnetic circuit 79

6.6 Positioning of the magnetic circuit at cyclotron facility 80

6.7 The predicted deflection of the beam in a 60.96 cm (24 inches) drift tube when given the magnetic field data from Table 6.2 82

6.8 The results from witness plates 83

LIST OF TABLES

Table		Page
1.1	Analogy between electric and magnetic quantity	5
2.1	The example of beamline requirement at CIAE	17
3.1	The characteristics of PETtrace Cyclotron	25
5.1	Circuit properties for 100 Amps, 50 x 2 turns	62
5.2	FEMM output at the center of the gap	63
6.1	The result of measurement using magnetic probe at the center of the gap	79
6.2	The approximation of magnetic field produced with 65% efficiency	81
6.3	Faraday cup reading	84

CONTROL AND CHARACTERIZATION OF A CYCLOTRON PROTON BEAM

Maslina Mohd Ibrahim

Dr. John Gahl, Thesis Supervisor

ABSTRACT

The cyclotron proton beam accelerator at the University of Missouri Research Reactor (MURR) is used for positron emission tomography (PET) applications. Pharmaceutical radioisotopes are produced and delivered to local hospitals for cancer diagnosis and nuclear imaging. The proton beam's energy is 16.5 MeV and the diameter of the beam is approximately 1 mm. A system to control the proton beam's position has been developed by using a magnetic coil. The position of the beam can be controlled to move in the *x* and *y* directions; with the beam in the *z*-direction. A Faraday cup was used as a diagnostic to monitor and characterize the beam after deflection. The system was designed by using magnetic circuit theory and fundamental electromagnetic theory. A software package called finite element method magnetic (FEMM) has been used as a simulation tool to conduct finite element analysis of the designed circuit. The beam steering experiment was conducted in two steps. First by using "low" and "high" current experiments in the laboratory and measuring magnetic fields produced. Then. by testing the magnetic circuit in the cyclotron facility at MURR. The beam was successfully deflected and the distant of the deflection can be control by the user by changing the value and orientation of the current used to drive the magnetic circuit.

CHAPTER 1

INTRODUCTION

1.1 Introduction

Cyclotrons have become one of the leading technologies for radioisotope production especially for medical applications. The development of radionuclide production for positron emission tomography and a negative ion cyclotron which extracts a proton had been discussed by Ruth [1]. The large numbers of cyclotron facilities in the world also have contributed towards this growth. However, every cyclotron facility has its own features, specifications and functionality. The cyclotron facility at University of Missouri Research Reactor (MURR) is dedicated to the production of isotopes for positron emission tomography (PET) application. One of the main isotopes produced is flourine-18 for use in fluorodeoxyglucose (^{18}FDG) [2].

^{18}FDG is an important drug that is used in connection with PET cameras that yield excellent quality images of the brain (for studying functional abnormalities), heart (for studying viability function) and tumors (for detection of metastases). Recently, MURR

also has been producing copper-64 that is extracted from a solid target [3-5] which is relatively more complicated compared to the liquid target for flourine-18.

The most important part of the cyclotron facility is its emitted beam. The beam of the cyclotron has a direct impact on the production of radioisotopes. This is why many research and production projects have been focusing on controlling and manipulating the beam. In this thesis, we are concentrating on steering the proton beam at the cyclotron facility at MURR. Fundamental and applied physics have been used for this purpose and the subsection below briefly discusses these important topics.

1.1.1 Charged Particle Beam

Charged particles that are commonly used for various applications are electrons or ions. The electron is an elementary particle and the proton is the simplest ion, a hydrogen atom with its single electron removed. Electrons and protons are elementary particles with the following characteristics:

$$q_e = -e = -1.602 \times 10^{-19}\ C \qquad m_e = 9.109 \times 10^{-31}\ kg \tag{1.1}$$

$$q_p = +e = +1.602 \times 10^{-19}\ C \qquad m_{ep} = 1.673 \times 10^{-27}\ kg \tag{1.2}$$

For charged particles to be a beam, the following condition must be fulfilled:

- The particles travel in almost the same direction.
- The particles have a small spread in kinetic energy.

Several quantities are useful to characterize charged particle beams, including type of particle, average kinetic energy, current, power, pulse length, transverse dimension, parallelism and energy spread. More detailed information can be found in [6].

1.1.2 Magnetic Force and Moving Charge

Hendrik Lorentz (1853 –1928) introduced the Lorentz Force in 1892. The Lorentz force, $\boldsymbol{F}$, is described where moving charge with velocity v, on a magnetic field $\boldsymbol{B}$.

$$\boldsymbol{F} = q\boldsymbol{v} \times \boldsymbol{B} \tag{1.3}$$

The implications of this expression are that the force $\boldsymbol{F}$, is perpendicular to both the velocity v, of the charged particle and the magnetic field $\boldsymbol{B}$. The magnitude of the force is $F = qvB \sin\theta$ where the angle θ, is between the velocity and the magnetic field and less than 180 degrees; and the direction of the force is given by the right hand rule.

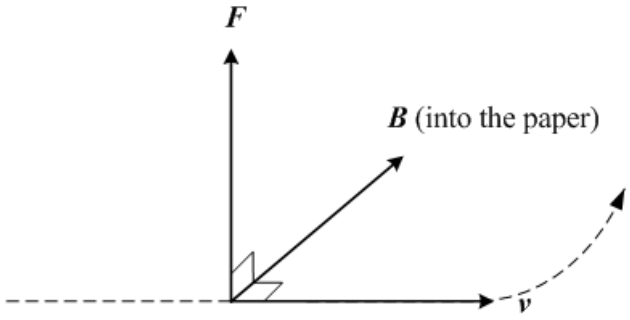

Figure 1.1: The right hand rule and the motion of a particle when the charge moves in a uniform magnetic field

Figure 1.1 above shows that the magnetic force is perpendicular to both the magnetic field and the velocity according to the right hand rule. Perpendicular force will bend the path of the charge into a circle if the charge remains in the uniform magnetic field. The radius of that circle, *R*, can be written in term of mass of the particle, *m*, velocity of the particle, *v*, charged of the particle, *q*, and the magnetic flux, *B*, as in equation 1.4 below.

$$R = \frac{mv}{qB} \tag{1.4}$$

However, for a moving charged particle that doesn't remain in a magnetic field a moment of magnetic force will induce the charged particle with a transverse force that will bend or deflect the charged particle in a very small angle. The paraxial approximation, as described in the next section, can be applied to calculate the deflection of the proton beam line.

1.1.3 Paraxial Beam Transport with Space Charge

Beam focusing in accelerators can be described by knowing the beam transport equation. The beam at the cyclotron facility in MURR is cylindrical. The relationship between the radial components of the applied field to the axial field is:

$$E_r(r,z) = -\frac{\left(\frac{r}{2}\right)\partial E_z(0,z)}{\partial z} \tag{1.5}$$

$$B_r(r,z) = -\frac{\left(\frac{r}{2}\right)\partial B_z(0,z)}{\partial z} \tag{1.6}$$

The particles in cylindrical paraxial beams have a small transverse velocity, v_r, $v_\theta \ll v_z$. All particles have almost the same kinetic energy, $(\gamma-1)m_o c^2$, and axial velocity, $v_z/c = \beta$. Following the calculation methods by Humphries [6], we can derive the equation for axial variation of the envelope of a cylindrical beam:

$$R^{"} = -\frac{\gamma' R'}{\beta^2 \gamma} - \left[\frac{\gamma^{"}}{2\beta^2\gamma}\right] R - \left[\frac{qB_z(0,z)}{2\beta\gamma m_0 c}\right]^2 R + \frac{\varepsilon^2}{R^3} + \left[\frac{q\psi_0}{2\pi\beta\gamma m_0 c}\right]^2 \frac{1}{R^3} + \frac{K}{R} \qquad (1.7)$$

The quantity R is the envelope radius of the beam. For the cyclotron at MURR, the radius is approximately 1 mm. The detail explanation of this equation can be found in [6].

1.1.4 Magnetic Circuit Design

The equivalency of magnetic and electric quantities is useful in defining and analyzing magnetic circuits. Table 1.1 below shows two groups of equations:

Table 1.1: Analogy between electric and magnetic quantity

Electric	Magnetic
$\nabla \times \mathbf{E} = -\frac{\partial \mathbf{B}_e}{\partial t}$	$\nabla \times \mathbf{H} = \mathbf{J}_{\mathrm{m}}$
$\mathbf{E} = \frac{1}{\sigma}\mathbf{J}$	$\mathbf{H} = \frac{1}{\mu}\mathbf{B}$
$\nabla . \mathbf{J} = 0$	$\nabla . \mathbf{B} = 0$

Since the mathematical expressions for the two fields are equivalent, we can define equivalences between the physical properties of the electric and magnetic fields. These equivalent quantities are:

$$\mathbf{E} \leftarrow\rightarrow \mathbf{H} \tag{1.8}$$

$$-\partial \mathbf{B}_e / \partial t \leftarrow\rightarrow \mathbf{J}_m \tag{1.9}$$

$$\mathbf{J} \leftarrow\rightarrow \mathbf{B} \tag{1.10}$$

$$\sigma \leftarrow\rightarrow \mu \tag{1.11}$$

In circuit theory we assumed that $-\partial \mathbf{B}_e/\partial t = 0$ and $\mathbf{J}_m=0$. Under these conditions, we get $\nabla \times \mathbf{E} = 0$ for electric circuits and $\nabla \times \mathbf{H} = 0$ for magnetic circuits. For electric circuits, an electric scalar potential V is defined from which $\mathbf{E} = -\nabla V$. Since $\nabla \times (\nabla V) = 0$, the potential V can be obtained. For magnetic circuits, a magnetic scalar potential V_m is defined from $\mathbf{H} = -\nabla V_m$. Since $\nabla \times (\nabla V_m) = 0$, the potential V_m can be obtained.

The relations $\nabla \cdot \mathbf{J} = 0$ for electric circuits and $\nabla \cdot \mathbf{B} = 0$ for magnetic circuits both indicate that the flux of J for electric circuits and the flux of B for magnetic circuits are conserved. For electric circuits, the current entering a volume is equal to the current exiting the volume as in "Kirchhoff's nodal law". The same applies for magnetic circuits, the flux entering a volume is equal to the flux exiting the volume which is equivalent to Kirchhoff's law. A current, I and magnetic flux, ϕ are defined in equations 1.12 and 1.13 below which are nonzero for an open surface.

$$I = \int_s \mathbf{J} \cdot \mathbf{ds} \tag{1.12}$$

$$\phi = \int_s \mathbf{B} \cdot \mathbf{ds} \tag{1.13}$$

The ratio of *V* to I is the resistance R of the electric circuit. The analogous quantity for the magnetic circuit is the ratio of NI to ϕ where N is number of turns. It is known as the reluctance and is denoted by the symbol $\Re$. The resistance is purely a function of the dimensions of the conductor and the conductivity. For a magnetic core of the same dimensions as the conductor, the reluctance can be obtained simply by replacing σ in R by μ. However, unlike σ for conductors, μ for magnetic materials is a function of the magnetic flux density in the material. This makes the reluctance analogous to a nonlinear resistor. Thus the complete analogy is:

$$\mathrm{R} = \frac{\mathrm{V}}{\mathrm{I}} \leftarrow\rightarrow \Re = \frac{\mathrm{NI}}{\phi} \tag{1.14}$$

This procedure for the calculation of magnetic circuits has some limitation. If the magnetic circuit is saturated (as described in the next section), the establishment of the equivalent electric circuit is much more complicated. The reluctance of iron is nonzero causing additional branches in the circuit and complicating the analysis.

1.1.5 Magnetic Properties of Materials

Magnetism in matter can be classified in three categories which are diamagnetic, paramagnetic and ferromagnetic. Diamagnetic materials have a relative permeability, μ_r slightly lower than one while the paramagnetic materials have a relative permeability, μ_r slightly larger than one. In practice we can consider many materials as having μ_r equal to

one. Examples of these types of materials are copper and aluminum. The third category that we are interested in is ferromagnetic materials. Ferromagnetic materials possess large relative permeability, μ_r.

Ferromagnetic materials are very important in electromagnetic application. One of the characteristics of these materials that must be considered when dealing with electromagnetic design is the relative permeability μ_r. Relative permeability μ_r, depends on the magnitude of the magnetic field intensity |**H**| in the material. This phenomenon is called nonlinearity in the material. Ferromagnetic materials such as iron and low carbon steels have their own B-H curve dependant on the purity of the material. The general B-H curve graph is shown in Figure 1.2.

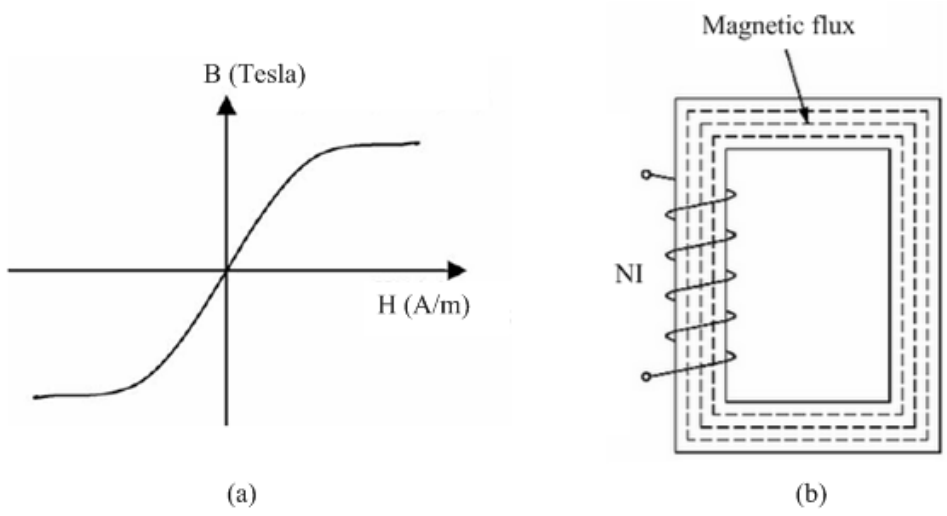

Figure 1.2: (a) B-H curve of ferromagnetic materials (b) example of magnetic circuit

From Figure 1.2 above, B is equal to ϕ/L where ϕ is the magnetic flux and L is the length of the magnetic flux path while H is equal to NI/l where N is number of turns, I is

the current in the wire and l is the length of the wire. This graph shows that for low currents, ϕ increases proportionally with I. At a certain value of I, the flux begin to increase at a different rate. In other words, saturation begins. This point is called the saturation flux density. In most electromagnetic applications, we want to avoid reaching the saturation of material since it accompanies a drop of inductance.

In this research, standard ANSI 1018 steel was used for cores. 1018 indicates the quantity of carbon in the steel, in this case 1.8%. Low carbon steel is one of the most commonly used steels for electromagnetic applications such as in transformer and magnetic circuits. Figure 1.3 below shows the B-H curve of ANSI 1018 steel.

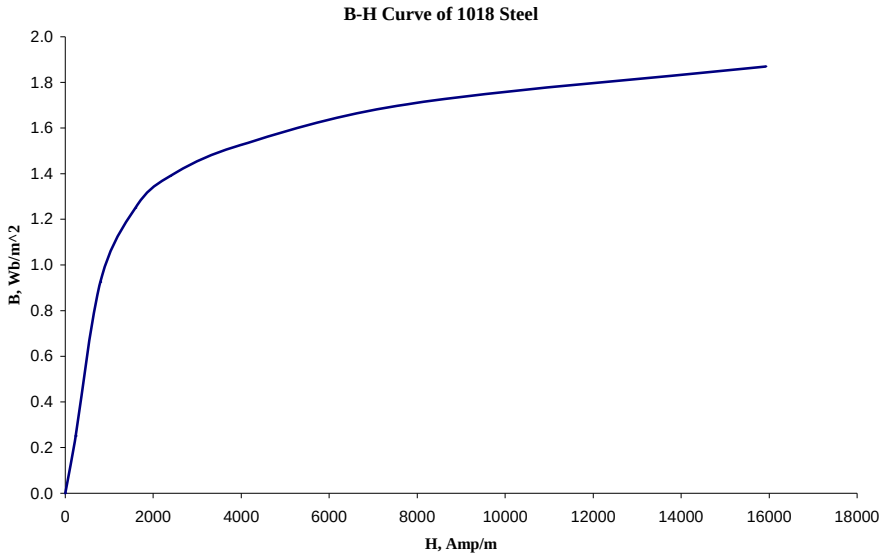

Figure 1.3: B-H curve of ANSI-1018 steel

From Figure 1.3 above, we can see that the magnetic field inside the steel should be less than 1.5 T in order for it to operate in the unsaturated state.

1.2 Research Goals and Intended Contribution

Our prime consideration in this research is how the proton beam of the cyclotron strikes the target for radioisotopes production. The object is to maintain a good production yield and ensure the longest useful lifetime of the radioisotopes. It is also important in attaining high specific activity (SA) of the radioisotopes. The production of the radioisotope can be not optimal if the beam didn't hit the target properly at the center. Even though the PET cyclotron at MURR already has its own targetry system, fine adjustment of the beam is not possible.

Every couple of months the cyclotron engineer calibrates the position of the beam manually by doing several tests at the cyclotron target. The calibration has to be conducted because the position of beam may change in time for several reasons. Some of the major factors are fouling of the ion source, ware and loosening of cyclotron components.

To increase production in targets producing florine-18 and copper-64, modifications of the existing target system must be made. This research applies magnetic circuit theory to manipulate the proton beam. The beam position can be adjusted in *x* and *y* direction by imparting a magnetic force on it. The protons in the beam can be given a force that will deflect their direction to the user's interest. By fine tuning the beam this way, we can have the maximum gain of isotope production. Figure 1.4 below shows how we define the position of the beam in this thesis. The Beam position is always assumed to be in the positive *z* direction or can be defined by $x\hat{x} + y\hat{y} + z\hat{z}$ where $x = y = 0$. The value of *x* and *y* are the magnitude of deflection.

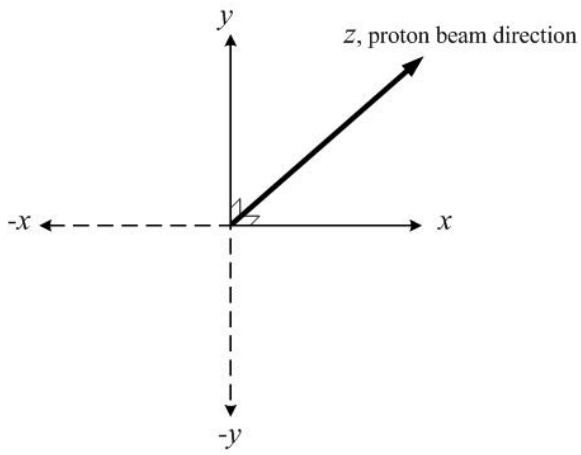

Figure 1.4: The position of the cyclotron proton beam

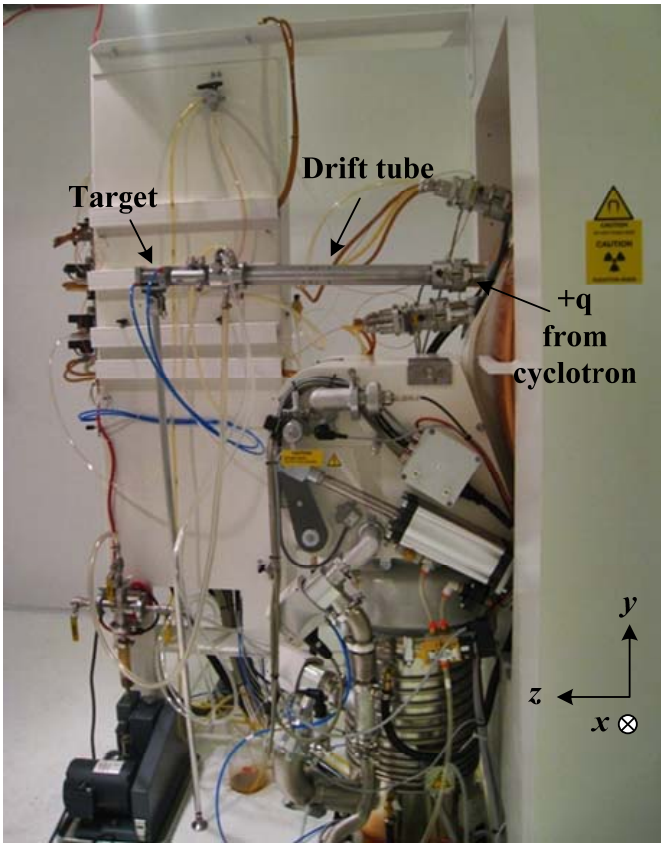

Figure 1.5: The side view of cyclotron machine at MURR

Figure 1.5 above shows the position of the target and the proton beam. The main objective of this research is to deflect the beam inside the drift tube to reach the target at the user's desired position. The target is roughly 10 mm in diameter; hence the design consideration is that the maximum deflection should not be more than this length. Since the beam is not always in the center, and may need to be deflected the full 10 mm.

In summary, the goals and intended contribution of this research are:

- To develop the magnetic circuit that can provide a uniform and sufficient magnetic field to deflect the proton beam.
- To prove that the beam has been deflected in accordance to the simulation and calculation.
- To provide an opportunity for further research regarding the effect of steering the beam to improve isotope production gain.
- To maximize gain of copper-64 in particular that is produced from a solid target that costs approximately $5000 per gram.
- To reduce the problem of hitting the solid target squarely. Since the target is so small and directly connected to the end of the drift tube of the beam, it easy to miss. The distribution of the beam through rastering can also reduce this problem.

1.3 Brief Description of Thesis Content

This thesis is comprised of seven chapters which are organized as follows. Chapter 1 provides the research topic background including charged particle beam, fundamentals principles of paraxial beam transport with space charge, magnetic force on moving charge, magnetic circuit design and magnetic properties of material. This is followed by the explanation of goals and intended contribution of this research.

Chapter 2 summarizes the previous work done to control and diagnose the cyclotron beams at other cyclotron facilities. The development and analysis of the magnetic circuit design is also summarized in this chapter.

Chapter 3 explains the fundamentals of cyclotron operation and relates it to the cyclotron facility at MURR. The beam and it functionality as well as magnetic safety considerations are also explained.

Chapter 4 starts with an explanation of the methodology used in this research. There are five important steps that were conducted from the beginning to the end of the research. Starting from the theoretical calculation to simulation and finally the experiment at the cyclotron facility itself is explained in detailed.

Chapter 5 deals with the simulation of the magnetic circuit by using a software package called finite element method magnetic (FEMM). The basic theory of how FEMM works is explained briefly. The results from this simulation are used as prediction values to measure the performance of the physical experiment that was conducted in the laboratory and in the cyclotron facility.

Chapter 6 consists of the results and discussion from the experiment that was conducted in the laboratory and in the cyclotron facility. The performance of the magnetic circuit when driven with “low” and “high” currents as well as the deflection of the cyclotron beam is thoroughly discuss in this chapter.

Finally in Chapter 7 the conclusion is drawn. Ideas for future work are also stated.

CHAPTER 2

LITERATURE REVIEW

2.1 Introduction

The cyclotron is a type of particle accelerator that has been used in many nuclear physic applications. Cyclotron technology can produce radioisotopes that are not possible to be produced by bombarding of isotopes using neutrons at a nuclear reactor. The yield of radioisotope production is closely related to the quality of the beam. Hence, this research is to improve and optimize the existing beam at the University of Missouri cyclotron facility, MURR. In the following sections we will present a brief review on the techniques currently been used for this objective.

The review is divided into two sections. The first section is a review of the techniques that had been used in cyclotron facilities to control and diagnose proton beams. Most of this research is targeted for specific applications of the beams. Examples of the efforts for controlling and characterizing proton beams by other institutes have also been highlight in this review. The following section is a description of the approach of this research. The magnetic circuit design has been conducted by using two techniques;

magnetic circuit theory and finite element analysis. The software package that has been used in this thesis is also introduced.

2.2 Review of Control and Diagnostic of Proton Beams

The most important part of a cyclotron system is it's beam. Hence, the study of controlling beams has been conducted since cyclotron technology has been available. The technology of beam control evolved depending on application and production mode. Positron emission tomography (PET) which is a nuclear imaging technique, is one of the applications that contributed the most in this area. The research and work regarding this had been conducted by nuclear research institutes as well as commercial companies.

There are several techniques used for controlling beams depending on how long the beamline is. The beamline is essentially an apparatus to transport the beam in a vacuum. For a long transport tube, a beamline uses quadrupole magnets and dipole magnets for control. M. P. Dehnel, *et al* described this technique which can defocus and focus beams. Much of his work lead to the development of commercial cyclotrons [7-10]. Typical beamlines that are discussed are in the range of 3 to 6 meters.

Another approach is the use of a short beamline as by J.E Theroux, *et al* [11]. This approach has many of the same capabilities as a long beamline where the beam position can be controlled and shaped by simply focusing the beam. This beamline utilizes an aluminum vacuum chamber, and graphite collimators to do the adjustment of the beam.

The design of the beam transport line and beam control are both dependent on the beam current and intensity as describe by S.Wei, *et al* [12]. The table below shows how the beam current and intensity of the beam varies for different applications at the China Institute of Atomic Energy (CIAE).

Table 2.1: The example of beamline requirement at CIAE

Requests for the beam of each line

Experiment terminal	Main purpose	Energy (MeV)	Intensity	Beam spot (mm)
N1	Beam dump and beam development	75–100	⩾200 μA	Φ40
N2	RIB production	75–100	20–200 μA	Φ4–Φ12
N3	Research related to Isotope production	75–100	100–200 μA	Φ10
S1	Neutron source 1	75–100	⩾200 μA	Φ15
S2	Neutron source 2	75–100	⩾ 200 μA	Φ25
S3	Biomedicine study	75–100	1–300 nA	Φ4–Φ30
S4	Proton irradiation facility	75–100	1–20 nA	Φ50–Φ300

M. P. Dehnel, *et al* also shows that PET Cyclotrons that mount targets directly at the periphery of the cyclotron vacuum chamber rarely have a system for centering or focusing the extracted beam on target to achieve maximum production [8]. This precludes the use of steering and focusing elements to adjust beam spot position and shape on target. The mounting of targets in a drift tube is one of the methods that allow us to develop a system to steer and control the beam.

There are several previous studies and projects to manipulate and control the beam position at different facilities. The Los Alamos Spallation Radiation Effects Facility (LASREF) has used a steering magnet and multi-wire harp to control the position of the

800 kW, 800 MeV proton beam on target [13]. Steering magnets have also been used in the Low-Energy Demonstration Accelerator (LEDA) at Los Alamos where two steering magnets were used in between the solenoid focusing magnets. [14-16]. At the Paul Scherrer Institute, a three-dimensional spot-scanning technique for radiotherapy with protons has been developed. Beam scanning uses a kicker magnet as a method to turn the beam on and off. A sweeper magnet is used to steer the beam [17].

There are many methods to diagnose and characterize cyclotron beams. The most common method is measuring the current and current density profile of the beam. Derenchuck mentions the use of a Faraday cup to measure the current of the beam to inspect the reliability and performance of the beam at the Indiana University Cyclotron Facility (IUCF) [18]. The use of a Faraday cup to measure the beam current has been conducted by many researchers due to its reliability and accuracy [19-22]. The Faraday cup has also been used for characterizationing proton beams in high resolution measurements [23, 24].

2.3 Magnetic Circuit and Finite Element Analysis

The most common approach to magnetic circuit design is the use of magnetic circuit theory. This technique allows researchers or engineers to design and analyze magnetic circuits by using electric circuit equivalents without too much complication. However, this approach ignores a lot of factors that will lead to inaccuracy of the designed models. One of the most important factors in magnetic circuit design is the nonlinear factor of magnetic saturation. As define by Tay, deep saturation is define as:

“For a closed iron circuit magnetized by a concentrated winding, deep saturation refers to a magnetization condition of the iron whereby the magnitude of the iron field B_m in the air-space begins decreasing as the magnetizing ampere-turns keep further increasing” [25]. This statement describes the saturation curve in materials also known as B-H magnetization curve. The B-H curve is used in almost every magnetic circuit design and each material has its own B-H characteristic. The characteristic B-H curve is often provided by the manufacturer; however a material’s B-H curve can also be found in the laboratory. Optimization using a B-H curve has been proven useful in previous studies [26]. The non-linearity saturation of the magnetic circuit has also been modeled by Moreau and Trigeassou [27].

The other approach for designing a magnetic circuit is to use a finite element analysis. This technique is more complicated but proves to provide a more accurate analysis of the magnetic circuit. Bell and Bodger compared magnetic circuit theory and finite element analysis techniques in the design of a power transformer and concluded that the finite element analysis technique gave a more accurate model. However, finite element analysis is more complicated and requires programming software [28]. Finite element analysis utilizes Maxwell’s equations and solves differential equations to operate. The details of these calculation have been describe by Shaffer [29].

Finite element analysis deals with the saturation problem as well as other parameters than cannot be easily calculated when using magnetic circuit theory. The analysis usually follows automatically after the finite element model is generated from new parameters. Since the B-H curve is also part of the finite element analysis, the effect of this curve is shown as contours in the flux patterns on the solid model [30].

Since finite element analysis has proven to be reliable and productive, many commercial companies offer software packages using it. For this thesis, an open source finite element analysis software package called finite element magnetic method (FEMM) was chosen [31]. The simulations of the magnetic circuit in this thesis were simulated in the FEMM software package. This software is well known to many researchers in the field because of it's reliability. FEMM has been used in the analysis and optimization of the magnetic behavior of various devices and systems [32-34].

This software package allows the user to choose; the type of material for each component, type of coil, number of turns of coils around the core, and electric current in the coils. These parameters are important in producing the magnetic field intensity H that is correlated with the magnetic flux density B. FEMM also allows us to use boundary conditions. The boundary condition used by FEMM is based on the paper by Qiushi [35]. This boundary condition approximates an open boundary condition by using asymptotic boundary condition theory.

2.4 Summary

We have discussed the techniques develop for focusing and steering proton beams. Techniques are always dependent on the application and need of the system. This thesis is aiming to improve an existing proton beam by allowing it to have a fine position function for improved control of where it strikes the target. Practical approaches to develop the magnetic circuit to steer the beam and the diagnostic system that will evaluate it have also been reviewed.

CHAPTER 3

CYCLOTRON

3.1 Introduction

The cyclotron was developed by Lawrence, Livingston and other researchers in the 1930's to accelerate heavy particles. The cyclotron consists of a large cylindrical chamber, placed between the poles of a huge electromagnet and is used for accelerating charged particles. The principle of the cyclotron is illustrated in Figure 3.1 below.

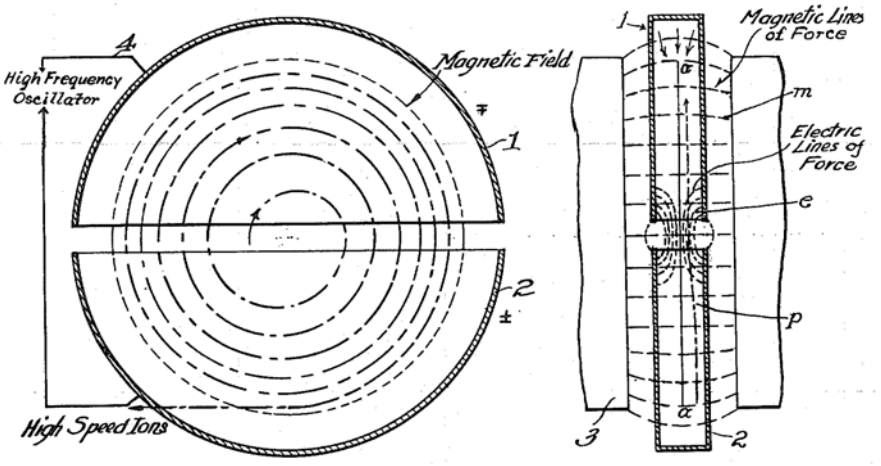

Figure 3.1: Principles of a cyclotron. U.S. Patent 1948384 [36]

The simplified explanation of figure above is that the particle with mass and charge moves with a velocity perpendicularly to the magnetic field and bend into a semicircular path between accelerations by an applied electric field. The applied electric field accelerates ions between the gap of the electrodes which are called "*dees*". The *dees* are labeled as “1” and “2” in Figure 3.1. The field is reversed at the cyclotron frequency to accelerate the ions back across the gap.

The cyclotron at MURR is an isochronous cyclotron type accelerator. This is actually a modification of a conventional cyclotron suggested by L.H. Thomas in 1938. The isochronous cyclotron is also called the azimuthally-varying-field (AVF) cyclotron and is classified among fixed-field alternating gradient (FFAG) accelerators. The delineating characteristic of this type of cyclotron is there is an increase in the angular velocity of the particles as the radius of curvature increases. This method requires the field distribution of the magnetic field to have a very high degree of accuracy. The field must increases radially in accordance with the particle energy. A method used to archive this is by modification of the conventional *dees*, instead of having plane-parallel surfaces; the pole faces of the *dees* are shaped. Figure 3.2 shows that the *dees* have magnetic valleys and hills.

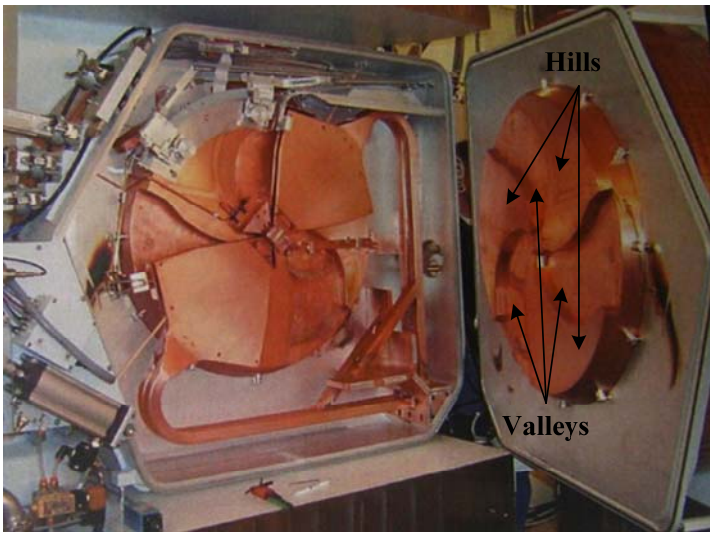

Figure 3.2: The *dees* of the cyclotron at MURR

3.2 PETtrace Cyclotron at MURR

The cyclotron at MURR is called PETtrace Radiotracer and was developed by GE. The accelerator is a fixed-energy isochronous cyclotron which accelerates negatively charged hydrogen ions (H^-) to 16.5MeV or negatively charged deuterium ions (D^-) to 8.4MeV energy. The total extracted beam current on target is approximately 100μA for protons and at least 60μA for deuterons. Figure 3.3 below shows the drawing of this cyclotron.

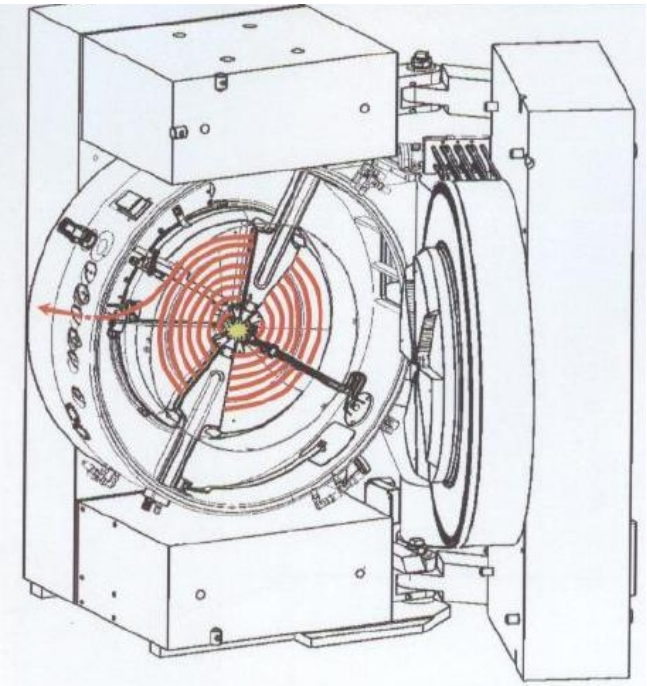

Figure 3.3: PETtrace radiotracer principle of operation

At the center of the chamber, an ion source (hydrogen ions H^- or deuterium ions D^- ions) is placed and emits ions. The *dees* are connected to a source of very high voltage radio frequency excitation (RF). When the cyclotron is in operation, the high frequency voltage will cause the electric charge on these *dees* to reverse rapidly. The particle will accelerate and travel in a nearly spiral path as in Figure 3.3 due to the alternating potential and the field of the electromagnet.

The particles become faster and require more energy each cycle. Finally, when they reach the outer rim of the chamber, the H^- or D^- ions are stripped of electrons, becoming positively charged protons or deuterons and then deflected toward a target. This cyclotron system has the capability of using 6 targets and various chemistry systems

for producing radioisotopes that are used in positron emission tomography systems (PET).

The characteristic of PETtrace cyclotron is summarized in Table 3.1 below.

Table 3.1: The characteristics of PETtrace Cyclotron

Proton Energy	16.5 MeV
Deuteron Energy	8.4 MeV
Beam current, extracted	- Protons >100 μA - Deuterons > 60 μA
Beam exit port	6

Currently only proton beams are extracted at the MURR cyclotron facility for radioisotope application. For the solid target system, each beam port used is connected with a beam drift tube. There are three different lengths that are currently being used in this facility; 15.24 cm (6 inches), 20.32 cm (8 inches) and 60.96 cm (24 inches). Figure 3.4 below shows the 60.96 cm (24 inches) beam drift tube connected to the beam port of the PETtrace cyclotron. The exploded view of the beam drift tube is shown in Figure 3.5.

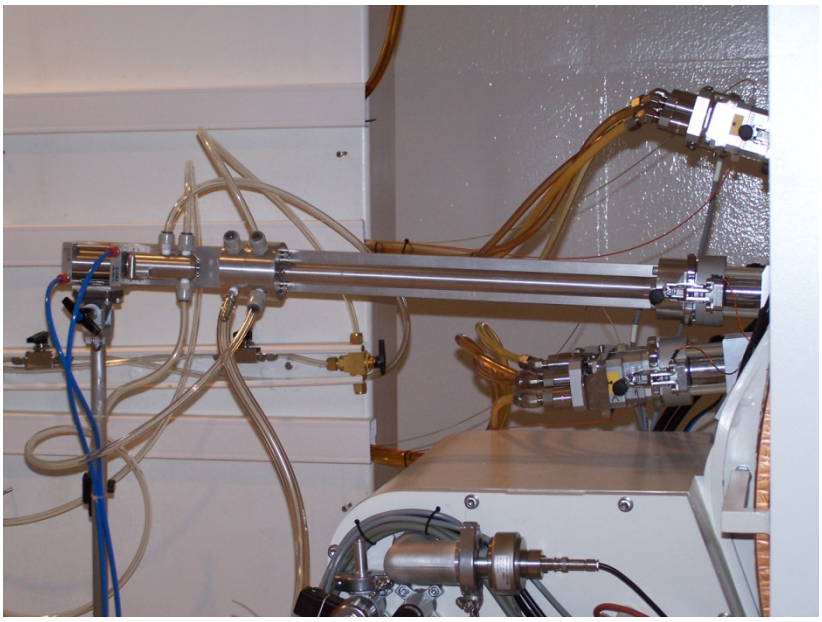

Figure 3.4: The 60.96 cm (24 inches) beam drift tube connected to the beam port of PETtrace cyclotron, MURR

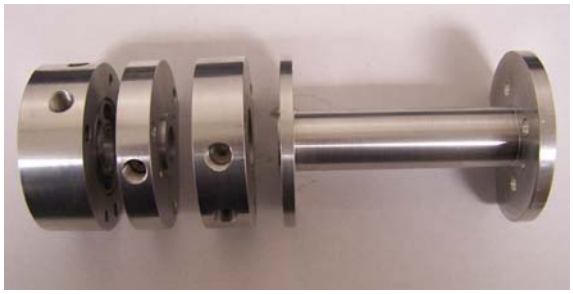

Figure 3.5: Exploded view of the beam drift tube

3.3 Magnetic Safety Consideration

When conducting the experiment at the cyclotron facility, one of the major concerns was the magnetic field produced from the cyclotron machine during operation [37]. Figure 3.4 below shows the surrounding magnetic field coming from the cyclotron machine. Since the magnetic circuit for the deflection is placed within one meter of the machine, the interaction between these two magnetic devices needed to be taking into consideration.

From Figure 3.6, we can see that the magnetic field within one meter is not less than 20 Gauss or 0.002 Tesla. In this thesis, we assumed that the magnetic field surrounding the deflection coil was 50 Gauss for simulation implementation. Another consideration regarding the magnetic field was the magnetic force between the cyclotron and our magnetic circuit. The magnetic coil should be affixed firmly and at the proper angle such that the beam and the magnetic force are perpendicular to each other to insure a maximum deflection.

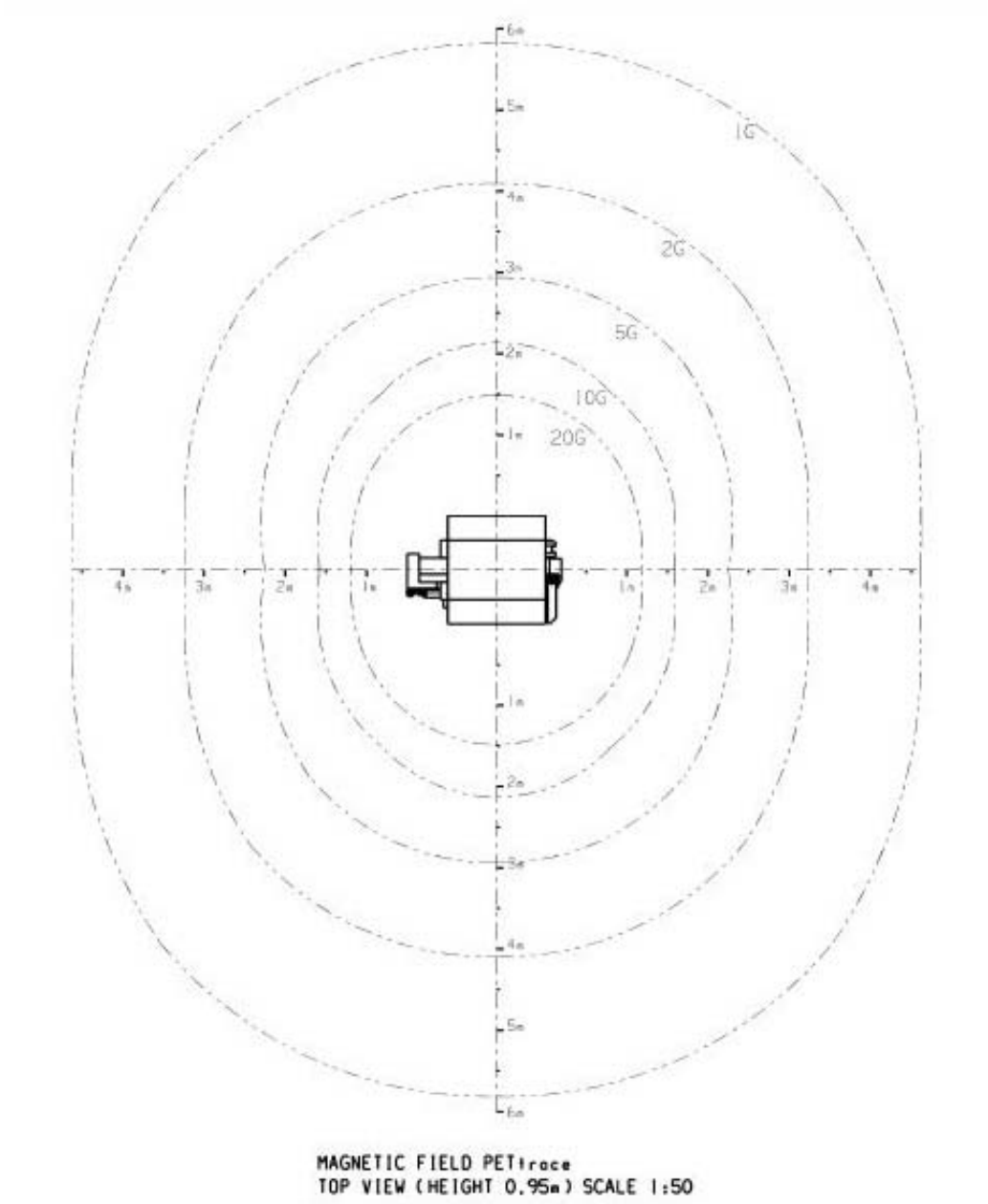

Figure 3.6: Magnetic field of PETtrace cyclotron at MURR – top view

CHAPTER 4

METHODOLOGY AND RESEARCH APPROACH

4.1 Introduction

The previous chapters gave the research background and presented the previous work conducted on proton accelerators in order to focus and steer beams. The previous work analyzing and developing magnetic circuits was also mentioned. This chapter will explain the research method and approach followed in this research. There are five important steps that have to be taken in order to complete the research.

First was the calculation of all the parameters from the beam that will affect the design of the steering system. The energy of the beam as well as the deflection distance is calculated in this stage. This step was important because it determined the force that will be provided from the magnetic field needed to deflect the beam.

The second step was the design of the magnetic circuit. The magnetic circuit was designed based on the output from step one. The design of the magnetic circuit is based on the suitability of it for use later at the cyclotron facility at MURR. In this step, we

determined what type of materials were to be used, current, resistance and all of the other parameters of the magnetic circuit.

The third step was the simulation of the magnetic circuit. Because of the many non-linear elements in this magnetic circuit, we needed another way of analysis instead of typical magnetic circuit theory. Further analysis of the magnetic circuit was conducted by using magnetic finite element analysis. A software package called Finite Element Method Magnetic (FEMM 4.2) was used for this purpose. FEMM provides information that cannot be easily found by the use of traditional magnetic circuit theory alone.

After we were satisfied with the results of simulations and analysis, the physical design of the magnetic circuit was implemented. This process involved the preparation of the magnetic core, power supply and the resistor. Since the current used for the magnetic circuit was quite high, close to 100 Amps, the power supply's amperage and regulation became a major concern.

Then, the final step was testing the system. At first the testing was conducted in the laboratory where low and then high current was applied to the magnetic circuit. From this we could see the pattern in the magnetic field data and compare it to the simulation data. We then tested the system on the cyclotron proton beam, with a simple Faraday cup and witness plate used to observe the deflection of the beam in response to the magnetic circuit.

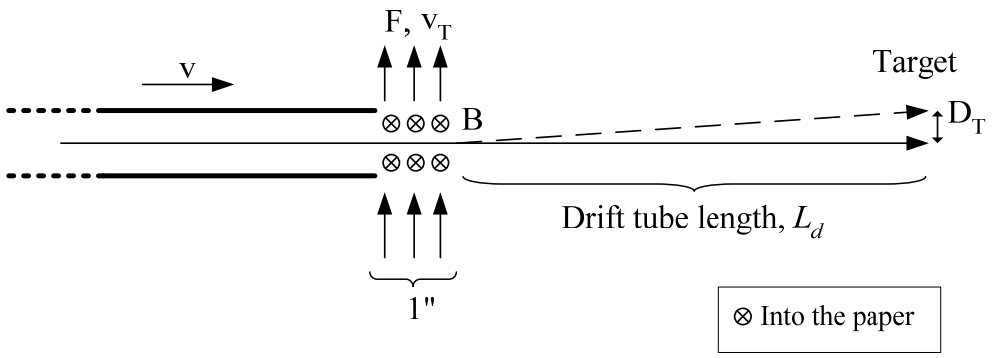

Figure 4.1: The schematic of the system

Figure 4.1 shows that protons in the beam are deflected by a distance, D_T in the **F** direction after going through the uniform magnetic field. The magnetic field in the one inch gap gives a perpendicular force that deflects the protons toward the direction of the force. The beam was shifted by this force along the length, L_d of the drift tube before finally reached the target.

4.2 Cyclotron Proton Beam Parameters Analysis

As mention in Chapter 3, the cyclotron proton beam at MURR has an energy of 16.5 MeV. From this, we can calculate the proton velocity, the transverse velocity after interaction with the magnetic field, and the drift distance or deflection distance. Since we designed the magnetic circuit to produce the magnetic field, the relationship between the magnetic field and the drift distance must be established.

4.2.1 Proton Particle Velocity

The proton velocity can be calculated by knowing the kinetic energy. Proton energy in the cyclotron beam is:

Proton energy = $16.4 \times 10^{6} eV \times 1.6 \times 10^{-19} C = 2.64 \times 10^{-12}\ J$

By ignoring the relativity factor, kinetic energy, *K*, of the proton can be written in term of mass, *m* and velocity, *v*, of proton. The mass of proton is 1.673 x 10^{-27} kg.s

$$K = \frac{1}{2} m v^2 \tag{4.1}$$

Hence;

$$\frac{1}{2} m v^2 = 2.64\ \times 10^{-12}\ J$$

$$v^2 = \frac{(2.64 \times 10^{-12})(2)}{1.673\ \times\ 10^{-27}}$$

$$v = \sqrt{3.1560 \times 10^{15}}$$

$$v = 5.6178\ \times 10^{7}\ \text{m/s}$$

By considering the relativistic factor, kinetic energy, *K* can be written as below where the relativistic factor is $\beta = v/c$ and *c* is the speed of light.

$$K = (\gamma - 1) m c^2 \tag{4.2}$$

$$\gamma = \frac{1}{\sqrt{1 - \beta^2}} \tag{4.3}$$

$$\beta = \frac{v}{c} \tag{4.4}$$

By using (4.2),

$$(\gamma - 1)mc^2 = 2.64 \times 10^{-12}\, J$$

$$(\gamma - 1) = \frac{2.64 \times 10^{-12}\, J}{(1.673 \times 10^{-27})(3 \times 10^8)^2}$$

$$(\gamma - 1) = 0.0175$$

$$\therefore \gamma = 1.0175$$

By using (4.3) and (4.4);

$$1.0175 = \frac{1}{\sqrt{1 - \beta^2}}$$

$$\beta^2 = 1 - \frac{1}{1.0175^2}$$

$$\beta = 0.184153$$

and;

$$v = \beta c$$

$$v = (0.184153)(3 \times 10^8)$$

$$v = 5.5246 \times 10^7 \text{ m/s}$$

Hence, the relativistic proton velocity in the cyclotron proton beam is 5.5246×10^7m/s.

4.2.2 Transverse Velocity

Transverse velocity is the velocity imparted on the proton in the perpendicular direction of the beam after interacting with the magnetic field. This velocity is in the direction of the force according to the right hand rule. To determine the transverse velocity, we have to measure the time the proton experiences this force. Hence, the transverse velocity, v_T can be written in the form of force, F, time in magnetic field, t_B, and the proton mass, m_p.

$$v_T = \frac{F \times t_B}{m_p} \tag{4.5}$$

The force on the proton and the time the proton is in the magnetic field can be calculated from the value of proton velocity calculated in Section 4.2.1. By using the Lorentz force equation, we can determine the force, $\boldsymbol{F}$ in term of proton velocity, v, magnetic field, $\boldsymbol{B}$ and charge, q as in equation (4.6):

$$F = q\,(\boldsymbol{v} \times \boldsymbol{B}) \tag{4.6}$$

Hence, the force received by the protons in the perpendicular direction is:

$$F = qvB \sin 90^o$$

$$F = qvB$$

$$F = (1.602 \times 10^{-19} C\,)(5.5246 \times 10^7\, m/s)B$$

$$F = (8.8504 \times 10^{-12} \times B)\, N$$

The other parameter needed is the time the proton is in the magnetic field. The time can be written in term of the velocity of the proton and the length of the magnetic field region as in equation (4.7). The length of the gap of magnetic core was determined to be 0.0254 m (1 inch).

$$t_B = \frac{L}{v} \tag{4.7}$$

Hence, the time the proton is inside the one inch magnetic field, t_B is:

$$t_B = \frac{0.0254\ m}{5.5246\ \times\ 10^7 m/s}$$

$$t_B = 4.5976 \times 10^{-10} s$$

$$t_B = 0.45976\ ns$$

Now we know that the protons will be in the magnetic field for 0.46 ns. By using (4.5), we can determine the transverse velocity of the proton.

$$v_T = \frac{(8.8504\ \times 10^{-12}\ \times B)\ \times\ 0.45976\ \times 10^{-9}}{1.673\ \times 10^{-27}}$$

$$v_T = (2.432193\ \times 10^6\ B)\ \text{m/s}$$

4.2.3 Transverse Distance

The deflection or transverse distance, D_T is the drift distance of the proton after reaching the target. The deflection from the Lorentz force bends the path of the charged particle into a circle when the charged particle passes through uniform magnetic field.

However, the protons in the beam only go through the magnetic field for approximately 0.46 ns, resulting in a very small angle deflection as shown in Figure 4.2. Hence, the transverse distance can be written as a function of transverse velocity, v_T and the time the proton takes to reach the target, t_D.

$$D_T = v_T \times t_D \tag{4.8}$$

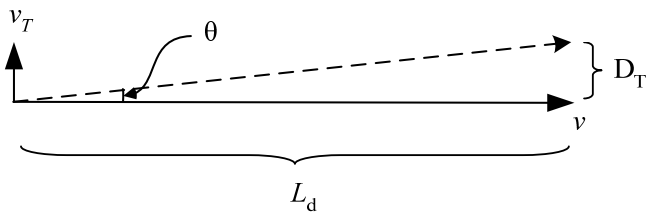

Figure 4.2: The schematic diagram of how the transverse velocity affected the path of the proton

We know the transverse velocity, v_T from Section 4.2.2. To get the value of the time the proton takes to reach the target, t_D, we can use the same equation (4.7) as was used to calculate t_B. The difference now is for t_D, the value of L has to change to the length of the drift tube, L_d. As mentioned in Chapter 3, there are three lengths of drift tube that are available at cyclotron, MURR. By using equation 4.7, the values for t_D with respect to the length of drift tube are as below.

Length of drift tube, L_d (meter)	Time for proton to reach target, t_D (ns)
0.1524	2.7586
0.2032	3.6781
0.6096	11.0343

Now we can calculate the transverse distance, D_T as describe in equation (4.8).

$$D_{T1} = (2.432193 \times 10^6 B)(2.7586 \times 10^{-9})$$

$$\boldsymbol{D_{T1} = 0.006709\, B} \qquad (4.9a)$$

$$D_{T2} = (2.432193 \times 10^6 B)(3.6781 \times 10^{-9})$$

$$\boldsymbol{D_{T2} = 0.008946\, B} \qquad (4.9b)$$

$$D_{T3} = (2.432193 \times 10^6 B)(11.0343 \times 10^{-9})$$

$$\boldsymbol{D_{T3} = 0.026837\, B} \qquad (4.9c)$$

Equation 4.9(a) to 4.9 (c) is the final equation of the transverse distant for the three lengths of the beam's drift tube. 4.9(a), 4.9(b) and 4.9(c) represent the transverse distant of the proton beam for 15.24cm (6 inches), 20.32 (8 inches) and 60.96 (24 inches) lengths of drift tubes respectively.

The angle of the deflection can be estimated as well by using the paraxial approximation where $sin\ \theta \approx \theta$.

$$\theta = \frac{D_T}{L_d} \qquad (4.10)$$

4.3 Magnetic Circuit Design

The magnetic circuit was designed to produce a uniform magnetic field in the proton beam's drift tube that produces the force that deflects the beam in *x* and *y* directions. Figure 4.3 shows the two positions of the magnetic circuit. In this figure, *v* is in the direction of the beam. With the proton moving into the paper and by using the right hand rule, in Figure 4.3 (a), the force is in the positive-*y* direction. To deflect the beam down or in negative-*y* direction, we simply change the direction of the magnetic flux by changing the direction of the current. The same concept is applied when we want to deflect the beam in the *x* direction.

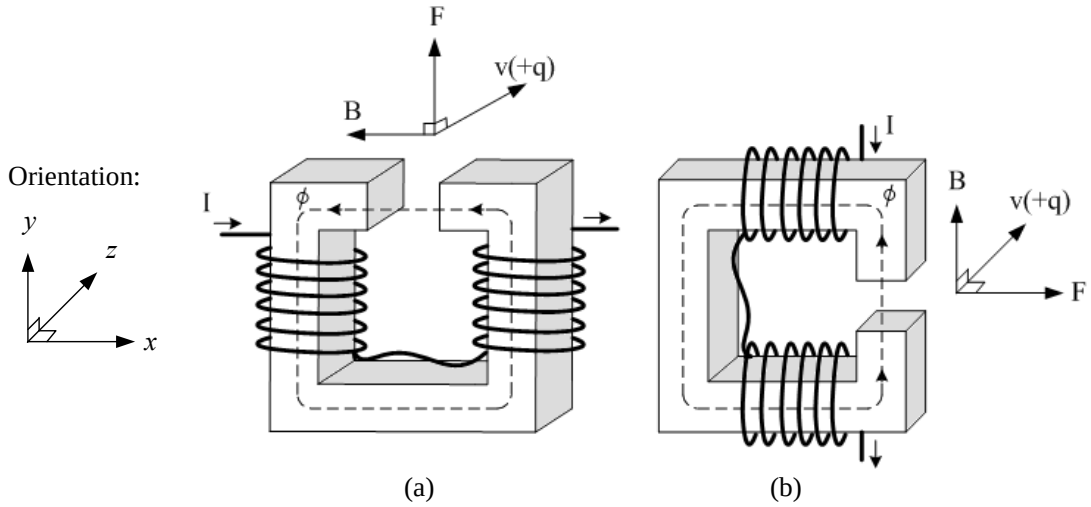

Figure 4.3: Illustrations of the magnetic circuit using the right hand rule (a) the force is directed in the *y* direction (b) the force is directed in the *x* direction.

To begin the process of designing the magnetic circuit, several factors should be taken into consideration such as; the nonlinear magnetic properties of steel, fringing of magnetic flux, possible losses at junctions and boundaries, limits on voltage, current, and/or inductance. To design the ideal magnetic circuit, low carbon steel or iron with a high magnetic permeability and saturation is desired. In this thesis, we designed the magnetic circuit based on available AISI-1018 steel which is an acceptable low carbon steel.

First, we determined the size of the air gap based on the diameter of the drift tube, which is 2.54 cm (1 inch). Figure 4.4 shows the dimension of the magnetic core that was used for this purpose. The magnetic core's dimensions were based on reasonable engineering design criteria so as to mount it on the drift tube and to wind the magnetic wire around it. Several cores with different dimensions were designed and computationally tested (Appendix), with the final design for the thesis is shown in Figure 4.4. The size of the magnetic core is 12.7 cm by 12.7 cm (5 x 5 inches) and the area of the magnetic flux is 2.54 cm by 2.54 cm (1 inch square). The length of the steel, l_s is 38.1 cm (15 inches) in total; whereas the length of the gap is 2.54 cm (1 inch). The cross sectional area of the gap, A_g and the steel, A_s is the same, which is 6.45 cm^2 (1 inch square)

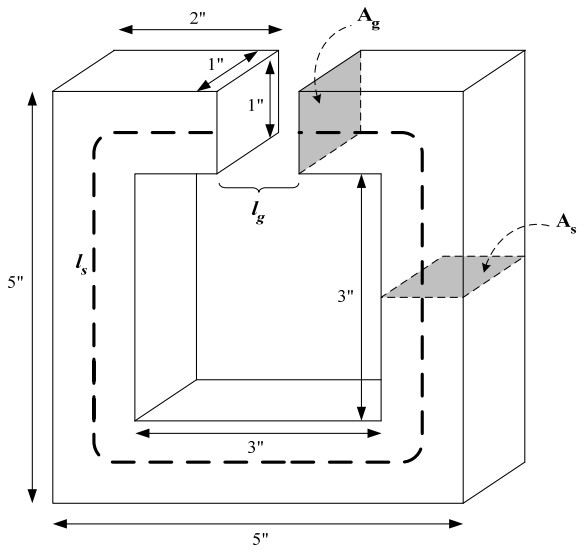

Figure 4.4: The dimension of magnetic core

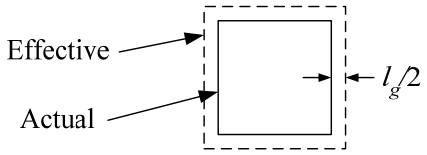

Figure 4.5: Effective (due to fringing) and actual cross section for the air gap

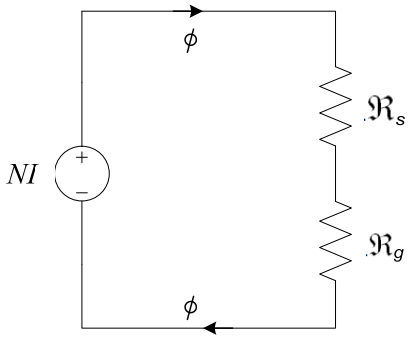

Figure 4.6: Equivalent circuit for analyzing the magnetic circuit

To analyze the magnetic circuit, we can visualize the circuit like an electrical circuit. Figure 4.6 shows the equivalent circuit for the magnetic circuit in Figure 4.3. Using Kirchhoff's law for magnetic circuits with the subscripts s and g referring to steel and gap respectively, we can write the following equations where H is magnetic field intensity and *l* is the length of the magnetic field in a medium:

$$NI = \oint H.dl$$

$$NI = \sum H_i.L_i$$

$$NI = H_s l_s + H_g l_g \tag{4.11}$$

Equation (4.11) can be rewritten by replacing the magnetic field intensity, H with magnetic flux, ϕ, permeability of material, μ and the area of the circuit, *A* as shown in Figure 4.4:

$$NI = \phi_s \frac{l_s}{\mu_s A_s} + \phi_g \frac{l_g}{\mu_g A_g} \tag{4.12}$$

$$= \phi_s \mathcal{R}_s + \phi_g \mathcal{R}_g$$

The objective of the magnetic circuit design is to achieve approximately 1 cm of deflection of the proton beam. By using equation (4.9c), we can determine the magnetic flux density needed at the gap.

$$B_g = \frac{0.01}{0.026817} = 0.373\,T\ (Wb/m^2)$$

From the calculation above, we will estimate the flux density at the gap to be 0.4 T. Now we can determine the total magnetic flux needed in the circuit by using the magnetic flux density, B and the cross section area, A, as the equation (4.13) below. For the area of the gap, we also have to consider the effective area instead of actual area due to the fringing factor [38]. Figure 4.5 shows the effective area for the air gap of the magnetic circuit. The effective area of the air gap is $(\sqrt{6.45} + l_g)^2 = 25.8\ cm^2$. The flux density in the air gap is therefore:

$$\phi_g = B_g A_g \tag{4.13}$$

$$\phi_g = \left(0.4\ \frac{Wb}{m^2}\right) \times (25.8 \times 10^{-4} m^2)$$

$$\phi_g = 1.032 \times 10^{-3} Wb$$

By using the principal of the continuity of magnetic flux, where $\phi_s = \phi_g$, the flux density for steel, B_s can be determined:

$$B_s = \frac{1.032 \times 10^{-3} Wb}{6.45\ \times 10^{-4}\ m^2} = 1.6\ Wb/m^2$$

The magnetic flux intensity, H in the air gap and in the steel can be determined. For the air gap:

$$H_g = \frac{B_g}{\mu_g} = \frac{B_g}{\mu_0} = \frac{0.4}{4\pi \times 10^{-7}} = 3.1831 \times 10^5 Wb/m^2$$

To find the magnetic flux for steel, H_s, one must refer to the B-H curve as in Figure 4.7 below. The value of H_s is 5200 amp/m.

From (4.11), we then have

$$NI = H_s l_s + H_g l_g$$

$$= (5200 \times 0.381) + (3.1831 \times 10^5 \times 0.0254)$$

$$= 10066\ amp - turns$$

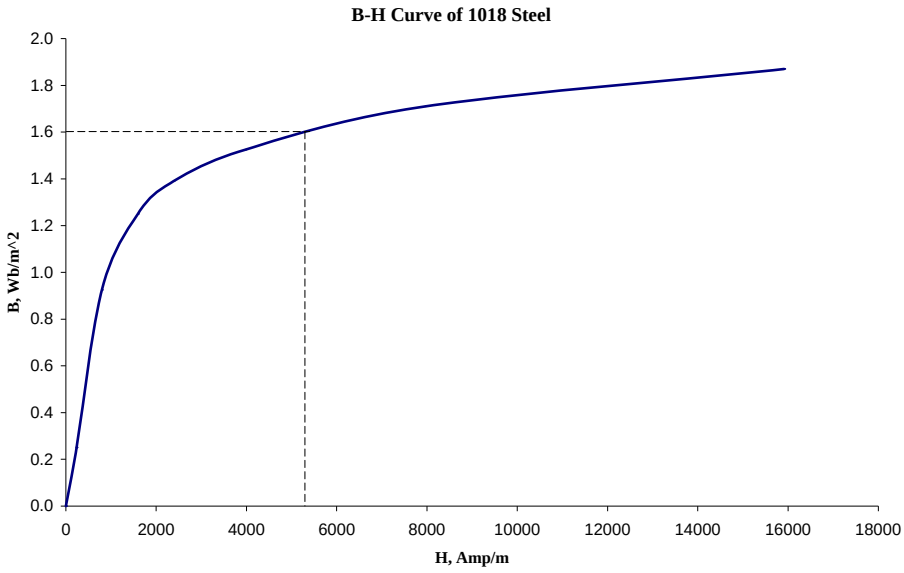

Figure 4.7: B-H curve for steel type ANSI-1018

Based on the calculation above, we can determine the number of turns and current needed in our magnetic circuit. For example, with 100 Amps of current, we need approximately 100 turns. The circuit is shown earlier in Figure 4.3 where the wire is wound on each side of the magnetic core instead of on the bottom of the core. The reason for this is the need for the coil to be as close as possible to the air gap to minimize losses. The magnetic wire used for this circuit is standard 10 AWG. This wire has a melting

point of 333 Amps [39]. At 100 Amps, some method of cooling needs to be used when the circuit is operated.

Another important factor to be considered is the type of steel for the magnetic core. It is ideal to use a very high permeability steel. This calculation is based on ANSI 1018 steel type, but if a different high permeability steel type was used, we should expect a small difference in the results.

4.4 Magnetic Finite Element Analysis

As explained on Section 4.3 above, we can calculate and estimate the performance of the magnetic circuit by using magnetic circuit theory. However, this calculation ignores many effects such as flux leakage and saturation of the material. To solve these problems, using finite element analysis is the ideal solution. Finite element analysis can calculate all these non-ideal effects as well as calculate the flux density, field intensity, and inductance using the numerical solution of Maxwell's equations and explicitly treating nonlinear materials. There is a number of software packages in the market that can do the finite element analysis for magnetic problems. This thesis uses a finite element analysis called Finite Element Method Magnetic Version 2 (FEMM 4.2), open source software by David Meeker [31]. The detail and analysis of this method will be discussed in the next chapter.

4.5 Implementation

Implementation of the experiment involved three processes. Firstly the experiment was conducted in a laboratory with low current, approximately 10 – 15 Amps. Then the experiment was conducted with high current, approximately 50 – 120 Amps. Finally the magnetic circuit was implemented in the cyclotron facility at MURR.

Figure 4.8 below shows the magnetic core that had been wound with 10 AWG magnetic wires. The magnetic field at the gap of magnetic circuit from the implementation in the laboratory was measured by using a 5170 Gauss/Tesla meter as shown in Figure 4.9.

Figure 4.8: Magnetic core with 50 turns of 10 AWG magnetic wires at each side

Figure 4.9: Magnetic field probe

4.5.1 Experiment Set-up

When setting up the experiment, one of the major concerns was current regulation and the power consumption by the circuit. For low current experiments, the power supply was operated with 5 V and 15 Amps. The circuit for the current supply is shown in Figure 4.10 below.

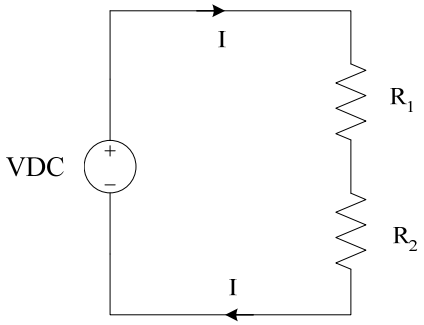

Figure 4.10: The circuit for low current source testing

R_1 is the resistance of the coil and R_2 represents the resistors in the circuit. R_2 is needed in the circuit as a resistance for the power supply. For the current to be 15 Amps, the total resistant, R_T and the power, P of the circuit are:

$$R_T = \frac{5V}{15A} = 0.333\ \Omega$$

$$P = 5V \times 15A = 75\ W$$

Resistance (ohms) per 1000 ft. in 10 AWG magnet wire is 0.9989Ω. The wire length needed is roughly 410 inches that give us the resistance of 0.0341Ω. Hence, the value of R_2 ($R_T - R_1$) is 0.2989Ω. To get this value, we used six 1.75Ω resistors in parallel. These resistors were rated at 30 W.

$$\frac{1}{R_2} = \frac{1}{1.75\Omega} + \frac{1}{1.75\Omega} + \frac{1}{1.75\Omega} + \frac{1}{1.75\Omega} + \frac{1}{1.75\Omega} + \frac{1}{1.75\Omega} = 3.428\Omega^{-1}$$

$$R_2 = 0.291\Omega$$

This gave us approximately 15 A of current for our low current testing. Power dissipation problem was not a problem since the total power that these resistors can handle in parallel is 6 x 30 = 180 Watt.

After we were satisfied with the result of the low current experiment, we continued the test by applying high current to the magnetic circuit. For this purpose, we used a power supply that was operated with 5V and 190 Amps. There were two main concerns when we start this experiment. First was the power was that produced and second was the resistance needed to control the current of the magnetic circuit. To solve both of these problems, we excluded the use of resistors; instead we used the coil itself as the resistance to the magnetic circuit. Since we were testing using a high current, we only needed a very low resistance. To get different values of current going through the coils, we just increased the length of wire from the power supply to the magnetic circuit.

The data from the low and high current experiment were taken to predict the performance of the magnetic circuit when used in the cyclotron facility. For the experiment inside the cyclotron facility, a stand for holding the magnetic core was designed as shown in Figure 4.11 below.

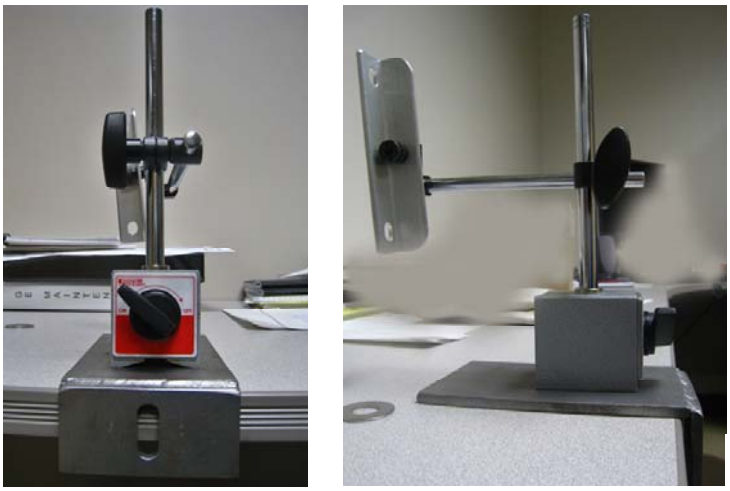

Figure 4.11: The stand for holding the magnetic circuit on the cyclotron machine

The magnetic circuit then was placed inside the cyclotron facility for the test as shown in Figure 4.12(a) and 4.12(b) below.

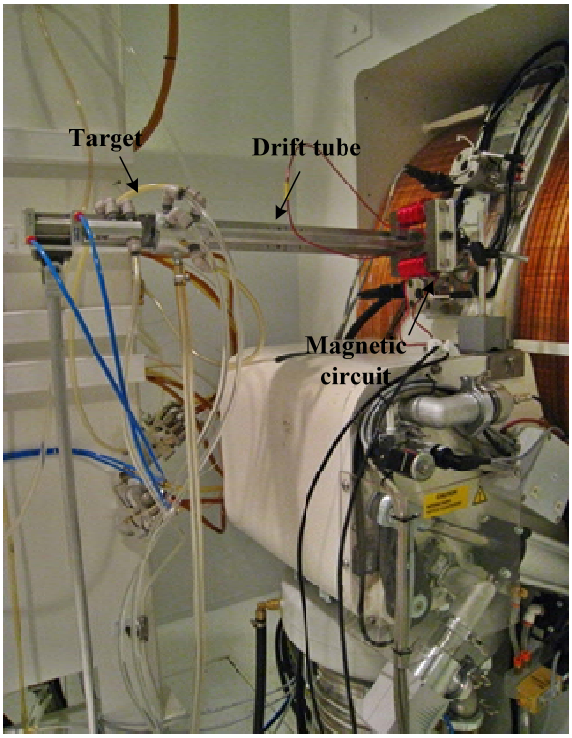

(a)

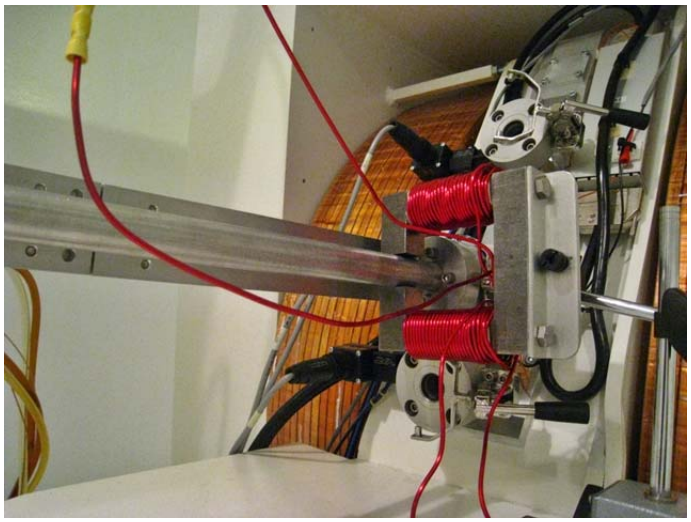

(b)

Figure 4.12: The magnetic circuit was placed at the beginning of the proton beam's drift tube (a) The whole view (b) Close up of the magnetic circuit

4.6 Diagnostic System

When the detection system was placed on the cyclotron beam, some sort of diagnostic system was needed to verify the deflection. The methods used were the measurement of the current from a witness plate and Faraday Cup.

The witness plate is simply a soft material that is put at the end of the beam drift tube as a target. The witness plate will show a burn mark when struck by the proton beam. This method allowed us to measure the distance of the beam deflection from it's original position.

The Faraday cup consists of two pieces of ceramic and one piece of aluminum plate. The aluminum plate has the diameter of 1.6cm and is placed in between the ceramics as shown in Figure 4.13. There are two steps in taking the data from the Faraday cup. First, the Faraday cup was assembled as in Figure 4.13(a) where the measurement was taken when the whole plate of aluminum was exposed to the beam. This first step was to make sure that the beam was on the target. After confirmation of the beam on target, the Faraday cup was configured as in 4.13(b) where only part of the aluminum plate was exposed. These two types of exposure are illustrated in Figure 4.14.

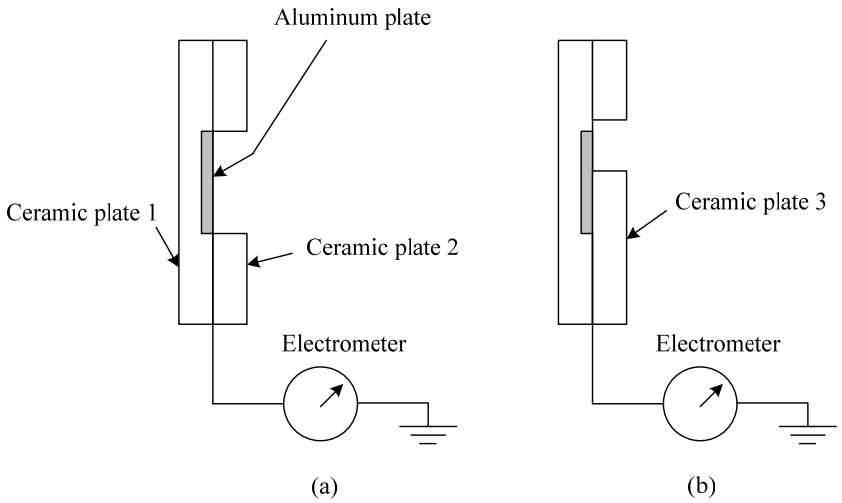

Figure 4.13: Schematic of Faraday cup (a) cross section for full exposure (b) cross section for partial exposure

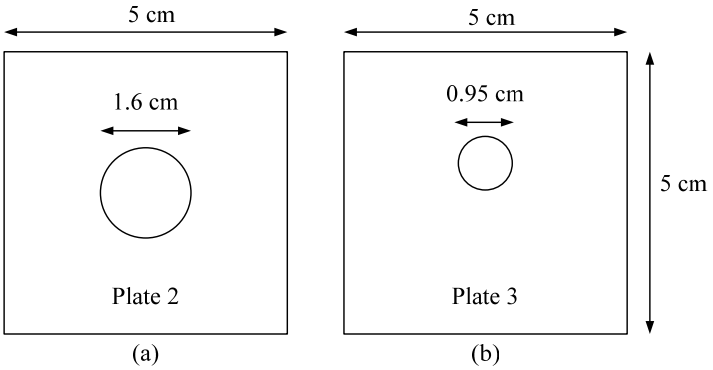

Figure 4.14: Ceramic plate (a) full exposure (b) one section exposure

Figure 4.15 below shows how we positioned the ceramic plate 3 to determine the position of the beam. When the beam hit the aluminum plate, we read the current from the meter that connected it to the Faraday cup. Based on the reading, we determined the position of the beam.

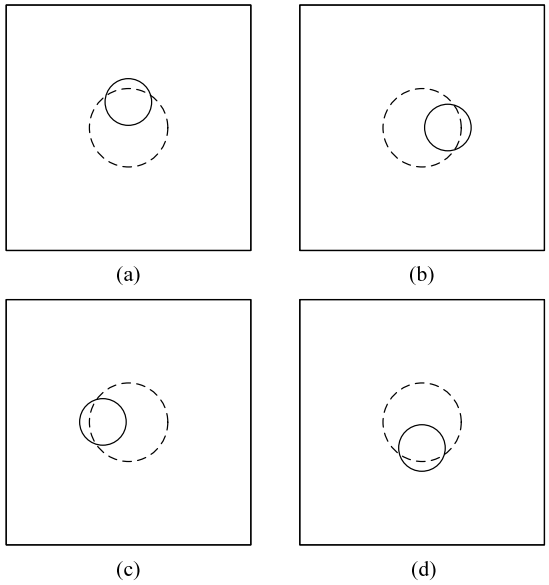

Figure 4.15: The placement of plate 3 to measure the position of the beam (a) top (b) right (c) left (d) bottom

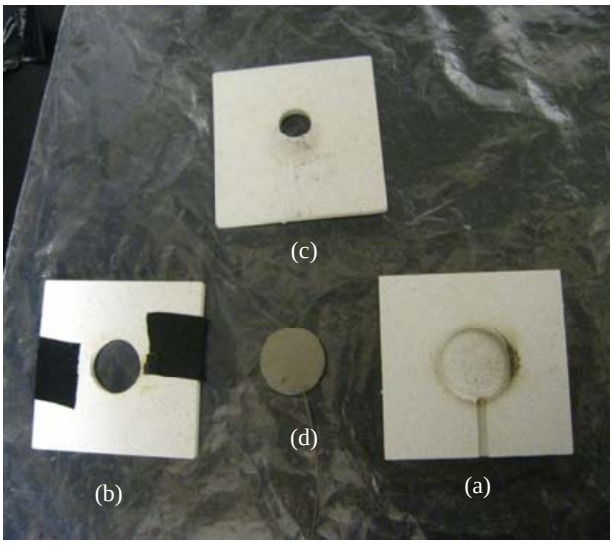

Figure 4.16: The Faraday cup (a) ceramic plate 1 (b) ceramic plate 2 (c) ceramic plate 3 (d) aluminum plate

CHAPTER 5

FINITE ELEMENT METHOD MAGNETIC

5.1 Introduction

Finite Element Method Magnetic (FEMM) is open source software that is distributed freely for use by those who are interested in electromagnetic problems. This software is mainly used to solve low frequency electromagnetic problems on two-dimensional planar and axisymmetric domains such as linear/nonlinear magnetostatic problems, linear/nonlinear time harmonic magnetic problems, linear electrostatic problems, and steady-state heat flow problems [32-34]. For the magnetostatic problem, the package is composed of an interactive shell encompassing graphical pre- and post-processing; a mesh generator; and various solvers that are useful for simulation and analysis of the problem concerned.

FEMM uses a numerical solution of Maxwell's equations via a magnetic vector potential approach for magnetostatic problems. The field intensity, H and flux density, B obey electromagnetic equations derived from static Maxwell relations as in (5.1) and (5.2) below:

$$\nabla \times \boldsymbol{H} = \boldsymbol{J} \tag{5.1}$$

$$\nabla \cdot \boldsymbol{B} = 0 \tag{5.2}$$

The constitutive relationship between B and H for material can be written as (5.3) below where μ is the permeability of the material:

$$\boldsymbol{B} = \mu \boldsymbol{H} \tag{5.3}$$

When saturation in material occurs, then the equation (5.3) becomes nonlinear, hence the permeability, μ become a function of B as (5.4):

$$\mu = \frac{B}{H(B)} \tag{5.4}$$

For the magnetic vector potential approach, flux density, B, is written in terms of the vector potential, A, as in (5.5) below. The advantage of using the vector potential formulation is that all the conditions to be satisfied have been combined into a single equation. If A is found, B and H can then be deduced by differentiating A.

$$\boldsymbol{B} = \nabla \times \boldsymbol{A} \tag{5.5}$$

Then, by using (5.5) and (5.4), (5.1) can be rewritten as:

$$\nabla \times \left(\frac{1}{\mu(B)} \nabla \times \boldsymbol{A} \right) = \boldsymbol{J} \tag{5.6}$$

For a linear isotropic material (and assuming the Coulomb gauge, $\nabla \cdot \mathbf{A} = 0$), eq. (5.6) reduces to:

$$-\frac{1}{\mu} \nabla^2 \boldsymbol{A} = \boldsymbol{J} \tag{5.7}$$

FEMM retains the form of (5.6), which is an elliptic partial differential equation, so that when saturation happens or when the B-H relationship becomes nonlinear, the problems can be solved.

Boundary conditions are very important in finite element analysis, and FEMM uses a boundary condition called *Robin*. An example of this boundary condition is:

$$\frac{\partial \boldsymbol{A}}{\partial n} + c\boldsymbol{A} = 0 \tag{5.8}$$

This boundary condition is defined as an "impedance boundary condition" that allow a bounded domain to mimic the behavior of an unbounded region [40].

After the boundary condition is defined, the idea of finite elements will be applied where the regions of the problem are broken into a large number of smaller regions to reduce the complication of the calculation. FEMM discretizes the problem domain using triangular elements. Over each element, the solution is approximated by a linear interpolation of the values of potential at the three vertices of the triangle. The linear algebra problem is formed by minimizing a measure of the error between the exact differential equation and the approximate differential equation as written in terms of the linear trial functions. An example of how the triangulation is conducted is show in Figure 5.1 where the map of Massachusetts is broken into small triangles. The smaller regions are made; the more accurate the solution can be.

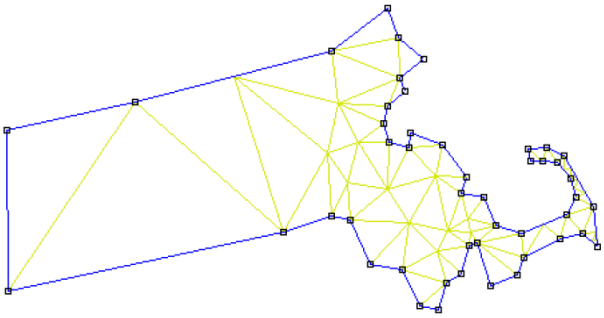

Figure 5.1: Triangulation of Massachusetts [40]

5.2 Model Construction and Design

The most important step to analyze the magnetic circuit using FEMM is to model the circuit in two dimensional geometry. Figure 5.2 shows the 2-D image of the magnetic circuit used in this research.

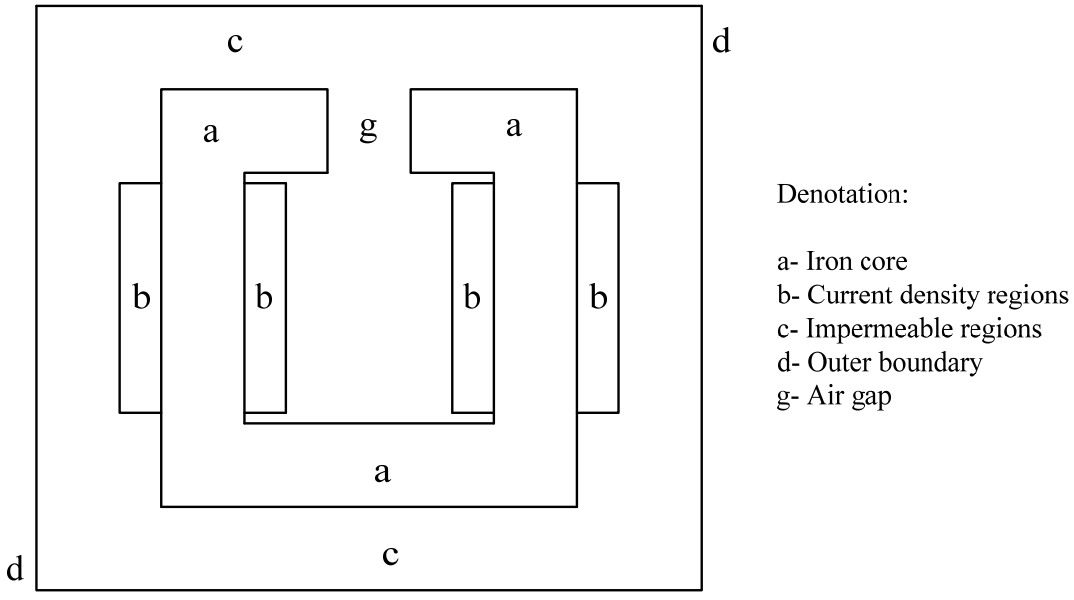

Figure 5.2: The 2-D geometry of the magnetic circuit regions

The cross sectional area of the core is one square inch. The gap length "g" of the magnetic core is 2.54 cm (1 inch). The circumference of the core is 50.80 cm (20 inches) with 12.70 cm (5 inches) on each side. The magnetic coil winding wire used is 10 AWG gauge. The diameter of this wire is 0.2588 cm (0.1019 inch). From Figure 4.9 above, the winding lies in the "b" areas, and consists of 50 turns of 10 AWG on each side. For 50 turns, only two layers of the magnetic coil were needed. The core extends for 2.54 cm in the "into-the-page" direction.

For the purpose of a finite element solution, the core is placed at the center of a 20.32 cm (8 inches) by 20.32 cm (8 inches) box. This box is set to be the boundary of analysis. The mesh size for triangulation is constrained to be no larger than 0.254 cm (0.1 inch).

Figure 5.3 below shows the meshed domain of the magnetic circuit. The material is set to be an ANSI 1018 steel and the area outside the core is set to air. The coil is wound in and out of the picture, with (+) and (-) symbols representing the direction of the winding of the coil.

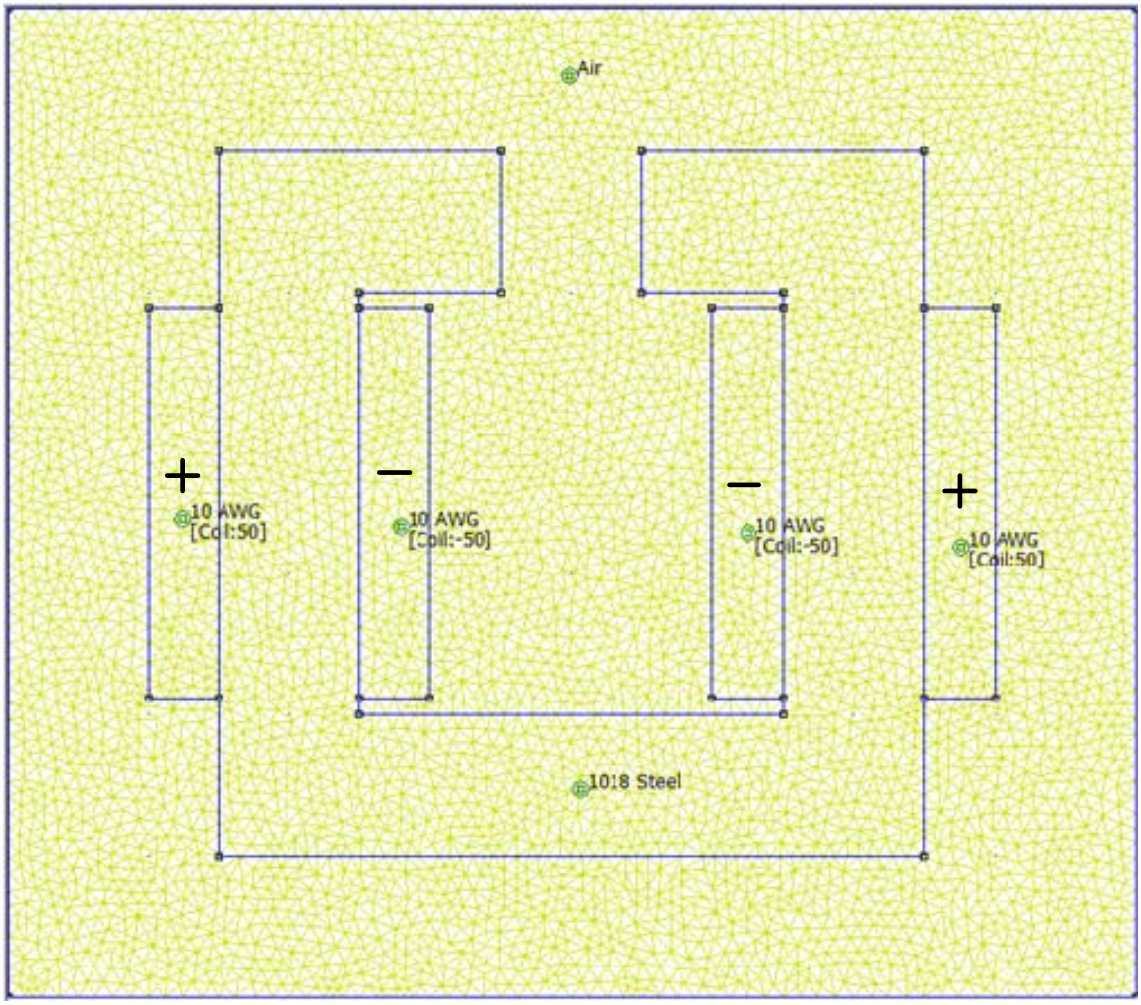

Figure 5.3: The meshed domain of the model

5.3 Boundary Condition

The boundary condition used is the technique describe in Chapter 2. This boundary condition will mimic the behavior of an unbounded region in a bounded region. The boundary conditions are important so that we can define the conditions for our specific problem. For this research, we used two types of boundary conditions. One is a "Mixed Boundary" condition type that approximates the impedance of an unbounded,

open space. In this way we can model the field produced by the magnetic circuit in an unbounded space while still only modeling a finite region. The coefficients for the mixed boundary condition are:

$$\frac{1}{\mu_r \mu_o}\frac{\partial A}{\partial n} + c_o A + c_1 = 0 \tag{5.9}$$

where A is magnetic vector potential, μ_r is the relative magnetic permeability of the region adjacent to the boundary, μ_o is the permeability of free space, and *n* represents the direction normal to the boundary condition. The parameters that need to be specified in this model are:

$$c_0 = \frac{1}{\mu_r \mu_o R}$$

$$c_1 = 0$$

where *R* is the radius of a spherical problem domain. For this model, the radius is set to seven inches.

The other boundary condition is the "Prescribe A". This boundary condition allows us to define the boundary when the magnetic circuit sits in a magnetic field. This represents the condition in the cyclotron facility at MURR where the magnetic field surrounding the magnetic circuit is approximately 50 Gauss or 0.0050 Tesla. The form A along the boundary is specified via the parameter A_0, A_1, A_2 and ϕ in the prescribed parameters box. These parameters correspond to the formula:

$$A = (A_0 + A_1 x + A_2 y)e^{j\phi} \tag{5.10}$$

Based on the FEMM document by Stoke-Rees [41] to analyze a block of iron sitting in a magnetic field, all of the parameters are set to 0 except A_0 and the unit of A_0 is Wb/m. To get 50 G or 0.005 Wb/m^2 of the magnetic field for the boundary condition with the length of 20.32 cm, A_0 is calculated as below:

$$A_0 = 0.005 \frac{Wb}{m^2} \times 0.2032\ m = 0.001016\ \frac{Wb}{m}$$

5.4 Simulation and Analysis on the Designed Magnetic Circuit

The modeling and the setting of the boundary conditions are the initial steps for the simulation and analysis of the designed circuit. The simulation from the FEMM will give us the value of magnetic field throughout the whole circuit where we can pin point the value of our interest. The simulation will also give us the circuit properties such as current, voltage drop, flux leakage and power. This will allow us to simulate the magnetic circuit in different settings for the observation and analysis of the circuit. Figure 5.4 below shows the simulation result at 100 Amps.

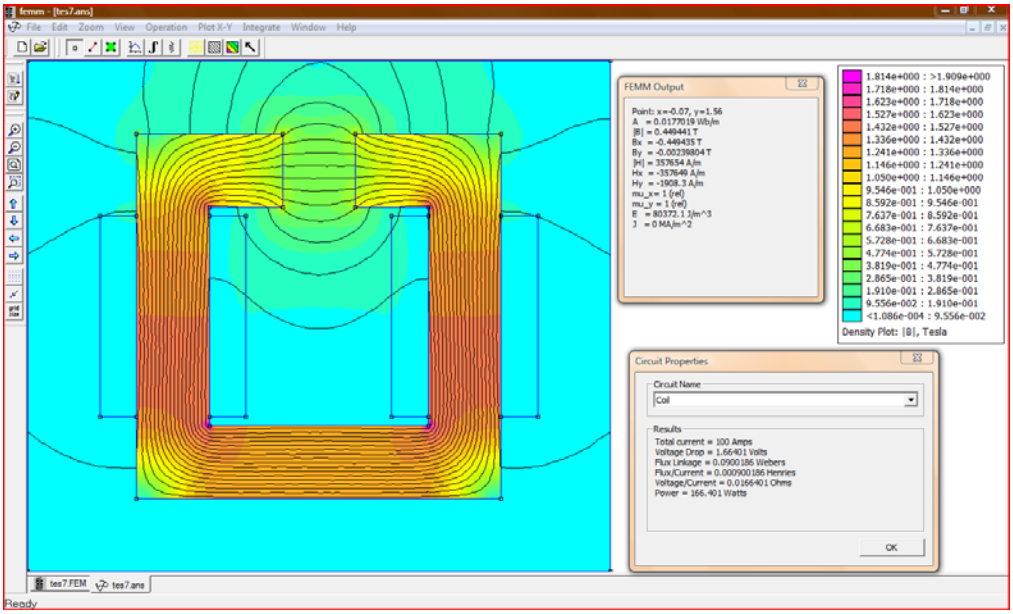

Figure 5.4: The simulation results at 100 Amps

The circuit properties and the output value at the center of the gap of the magnetic circuit above are as shown in the tables below:

Table 5.1: Circuit properties for 100 Amps, 50 x 2 turns

Total current	100 Amps
Voltage Drop	1.66401 Volts
Flux Linkage	0.0900186 Webers
Flux/Current	0.000900186 Henries
Voltage/Current	0.0166401 Ohms
Power	166.401 Watts

Table 5.2: FEMM output at the center of the gap

A	0.0183873 Wb/m
|B|	0.448673 T
Bx	-0.448673 T
By	-0.000202552 T
|H|	357042 A/m
Hx	-357042 A/m
Hy	-161.186 A/m
mu_x	1 (rel)
mu_y	1 (rel)
E	80097.6 J/m^3
J	0 MA/m^2

From the table above we can study the circuit properties and the output from this circuit at the center of the gap. For 100 Amps the circuit gives us a flux of 0.45 T. This will give us beam deflection of 0.30cm, 0.40 cm and 1.21 cm for 15.24 cm (6 inches), 20.32 cm (8 inches) and 60.96 cm (24 inches) long drift tubes respectively. As we can see, from the magnetic circuit theory calculation in Chapter 4, the H value for the gap was found to be 318310 A/m and from this simulation, the result is found to be 357042 A/m. The difference from the calculation and simulation result is 10%. The difference is largely due to the H value of the steel being non-uniform as assumed in magnetic circuit theory. In practice, the H value will change depending on the position of the coils in the circuit. Figure 5.5 shows the H-value profile for the magnetic core used in this thesis.

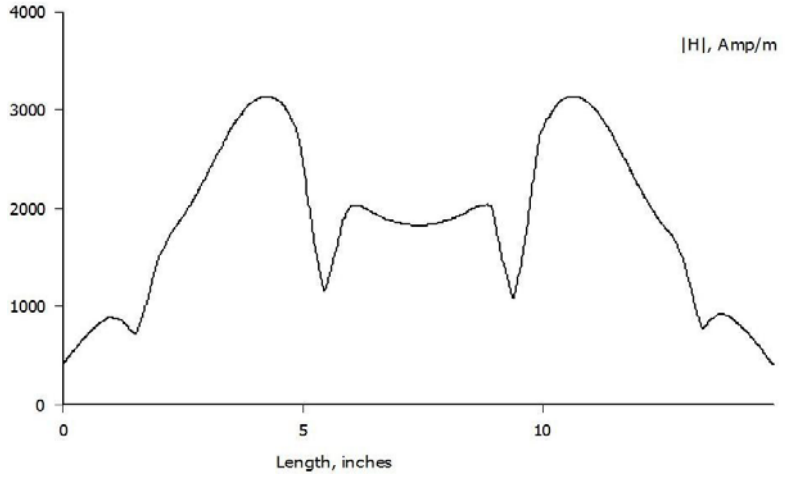

Figure 5.5: The H-value profile for the magnetic core

The graph above shows that the H value in the steel along the magnetic core changes depending on location from the coil. The two maximum peaks indicate the location of the two coils on the magnetic core. While the lowest point which is at the start and the end of the graph indicates the edge of the gap. This graph is proportional to the magnetic flux profile graph as shown in Figure 5.6 below. These observations prove the linearity of the B-H curve in Figure 4.7.

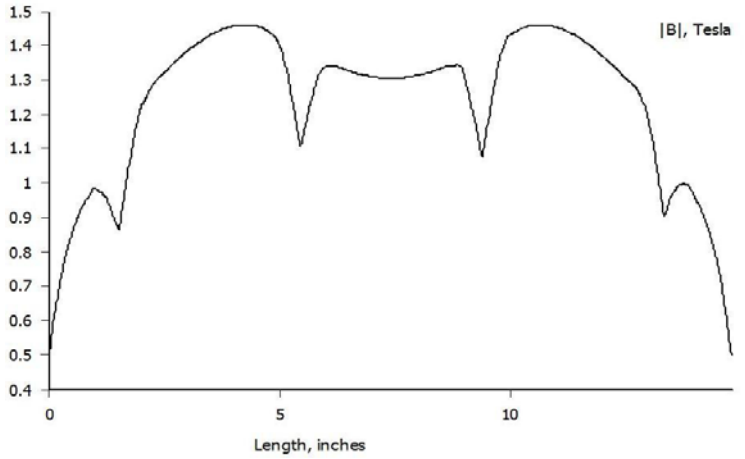

Figure 5.6: The B-value profile for 1018 steel magnetic core

Further analysis of the magnetic circuit was conducted by applying currents in the range of 0 to 350 Amps to the magnetic circuit. The result at the gap of the magnetic circuit is shown in Figure 5.7 below.

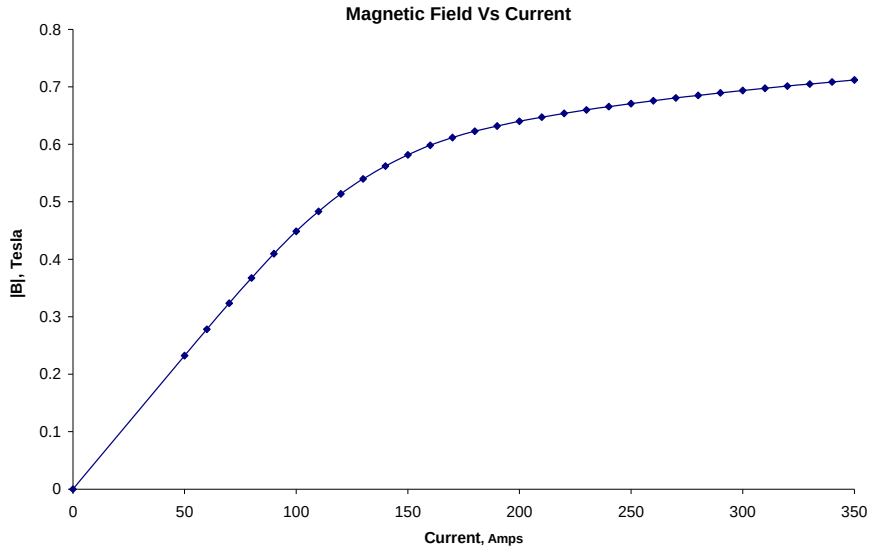

Figure 5.7: Magnetic field magnitude at the center of the gap with currents range from 0 to 350 Amps

From Figure 5.7, we can see that the magnetic field measurement shows the occurrence of saturation in the material when high current is applied. Saturation means that the magnetic field cannot be increase even though we increase the current at the coil. Hence, to optimize the power, we should only operate when the graph is linear. For this thesis, we will analyze using current between 0 to 170 Amps.

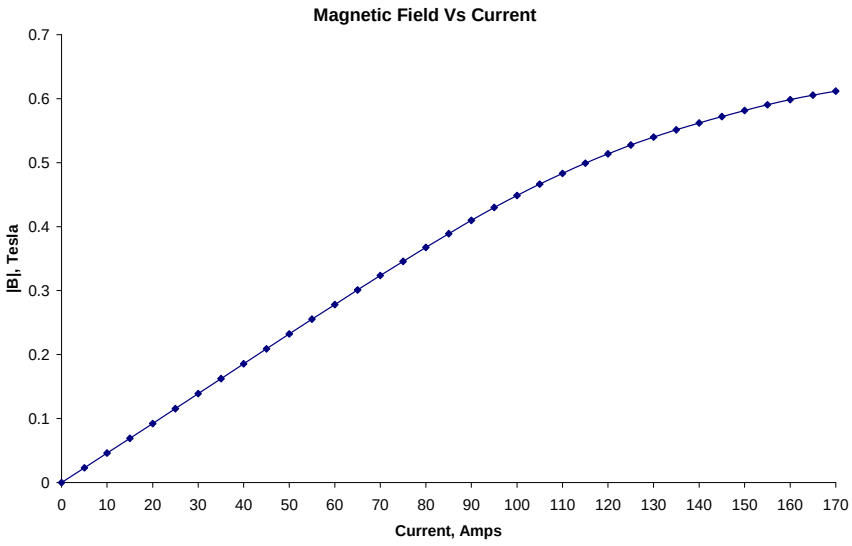

Figure 5.8: Magnetic field magnitude at the center of the gap with currents range from 0 to 170 Amps

The drift tubes that are currently used at the cyclotron facility at MURR have three lengths drift 15.24 cm (6 inches), 20.32 cm (8 inches) and 60.96 cm (24 inches). Figure 5.9 shows that with the longer drift tube, we can use a lower current for the deflection. Since the target size is approximately one cm, the 60.96 cm tube will give us the maximize deflection at only 80 Amps of current.

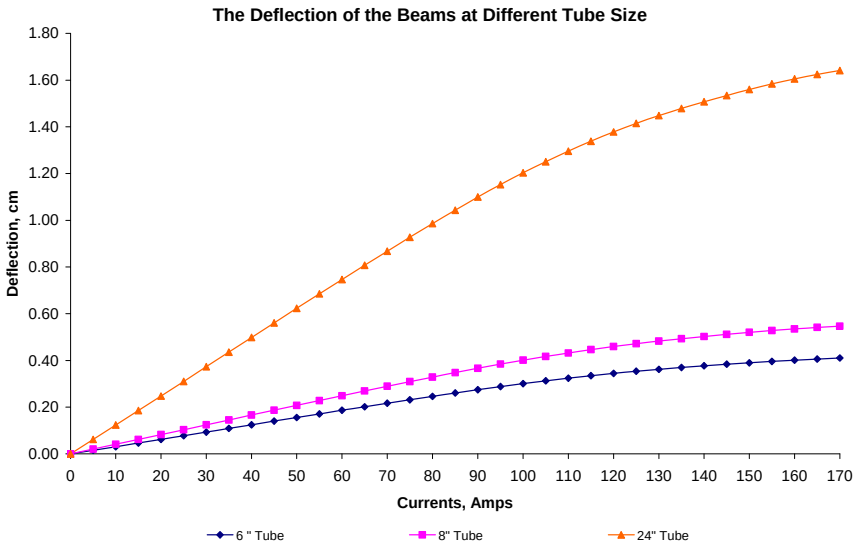

Figure 5.9: The deflection of the beams at different tube size

5.5 Analysis of Magnetic Circuit in the Magnetic Field Environment

The analysis for a field free space is necessary to predict the experiment's result in the laboratory as in Section 5.4 above. However, in practice the magnetic circuit will be placed inside the cyclotron facility where the surrounding environment is not a normal field free space like in the laboratory. The cyclotron has magnetic field leakage from its own magnet. According to the PETtrace cyclotron manual [37] as explain in Chapter 3, the magnetic leakage within the one meter surrounding is no less than 20 G (0.002 T). Since the magnetic circuit will be placed very close to the machine and inside the one meter area, we assumed that the magnetic field surrounding the magnetic circuit is 50 G (0.005 T).

From Chapter 4 in Section 4.3, it is explained that the magnetic circuit will be placed in two different positions in order to change the direction of the beam. Since the cyclotron magnetic field has its own orientation, we have to consider the direction of this field. Depending on the placement of the magnetic circuit, the additive effect of the cyclotron magnetic field to the magnetic circuit will be determined. The simulation in FEMM was conducted with two different directions of cyclotron magnetic field as shown is Figure 5.9 and 5.10 below.

Let us consider that the magnetic field from the cyclotron is in the *x* direction. Figure 5.10 shows the field lines when the force of magnetic circuit is in *y* direction and Figure 5.11 shows the field lines when the force of magnetic circuit is in *x* direction. The direction of the cyclotron magnetic field changes the magnetic flux of the core of magnetic circuit slightly. The difference of these results is shown in Figure 5.12.

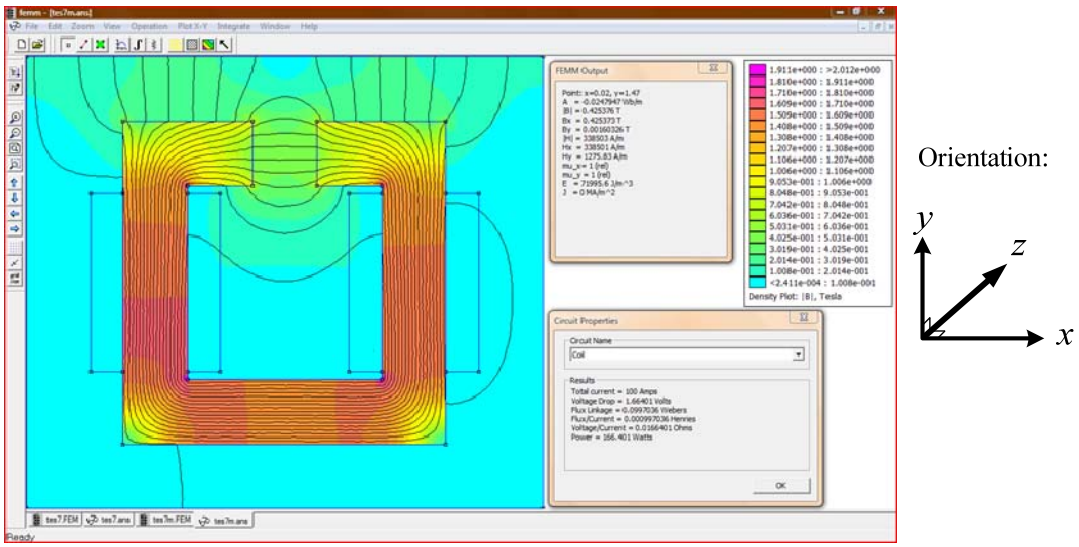

Figure 5.10: The simulation at 100 Amps where the force is in the *y* direction and the surrounding magnetic field is 0.005 T

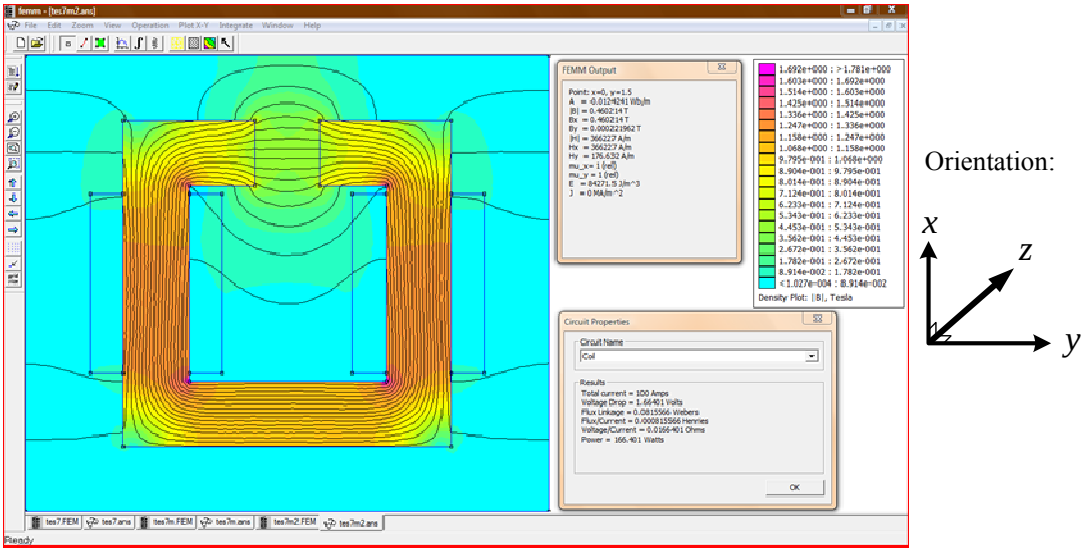

Figure 5.11: The simulation at 100 Amps where the force is in the *x* direction and the surrounding magnetic field is 0.005 T

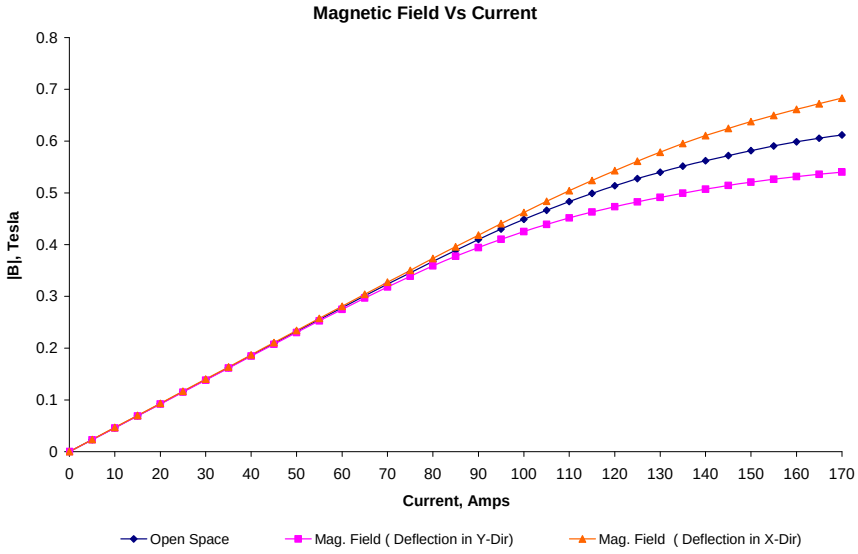

Figure 5.12: A comparison of the magnetic field at the gap of the magnetic core between field free and cyclotron magnetic field environments with *x* and *y* deflection direction

From Figure 5.12, we can see that between 0 to 85 Amps, the surrounding magnetic field doesn't impact the magnetic flux of the magnetic circuit. It only starts to significantly affect it when we increase the current to more than 85 Amps. The direction of magnetic field will either increase or decrease the magnetic field produced from the magnetic circuit when compared to the field free condition.

Based on the calculations from Chapter 4, we can predict the deflection of the beams depending on the length of the drifts tube. At MURR, we have three different lengths of drift tube and each of the lengths will give a different deflection value. Figure 5.13 to 5.15 below shows the results for each drift tube in the cyclotron environment.

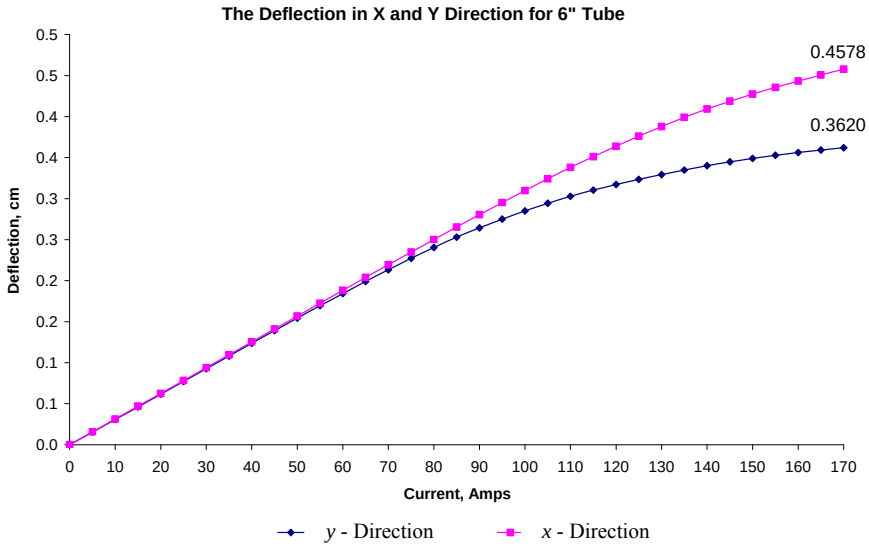

Figure 5.13: The deflection result for the current range between 0 to 170 Amps for 15.24cm (6 inches) drift tube

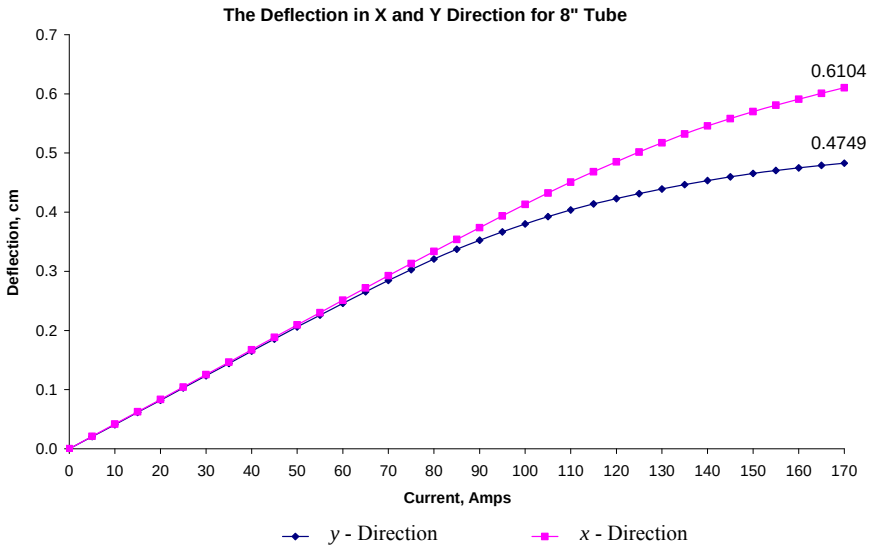

Figure 5.14: The deflection result for the current range between 0 to 170 Amps for 20.32cm (8 inches) drift tube

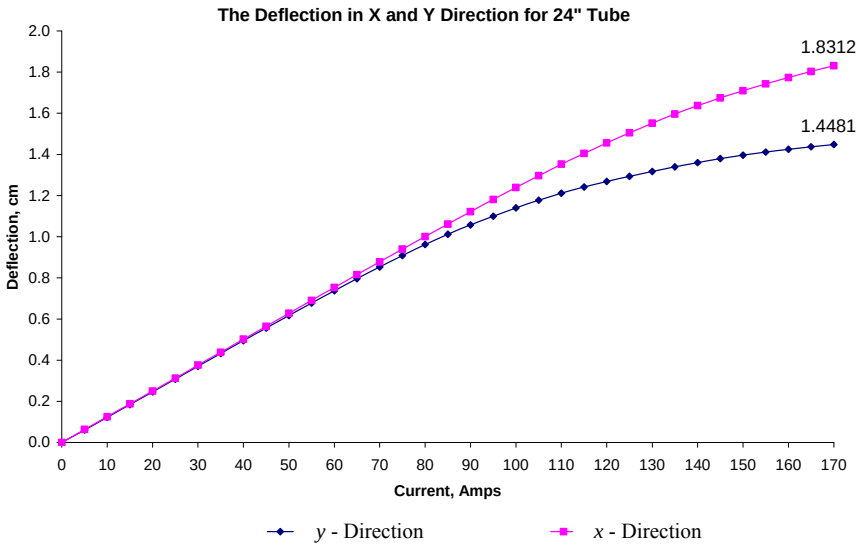

Figure 5.15: The deflection result for the current range between 0 to 170 Amps for 60.96cm (24 inches) drift tube

The deflection distant is greater with longer lengths of drift. Hence, with a longer drift tube, we can reduce the current and optimize the power while reducing the heat generated from the magnetic circuit. As shown in Figure 5.9, the longer drift tube will give us a better option to control the cyclotron beam.

CHAPTER 6

RESULTS AND DISCUSSION

6.1 Introduction

The previous chapters explained how we conducted the calculation, simulation and implementation of the magnetic circuit to deflect the cyclotron beam in the *x* and *y* directions. This chapter will continue with experimental results and a discussion of the actual performance of the magnetic circuit in the laboratory and in the cyclotron facility. The experiment was conducted in three tasks. The first two tasks were conducted in the laboratory while the last part of the experiment was performed in the cyclotron facility at MURR.

First, the experiment or the preliminary experiment on the magnetic circuit was conducted by using a low current. The characteristic of the magnetic field of the magnetic circuit were determined and compared to the simulation result.

After the experiment with low current, higher current was applied to the magnetic circuit. The current that was used in this experiment was almost the same as the current that would be used in the real cyclotron facility. The experiment was conducted at several

currents between 50 Amps and 120 Amps. The temperatures of the wires were also measured at all times while conducting the experiment at this level.

The final task was the test of the magnetic circuit at the cyclotron facility. The stand to hold the magnetic circuit was designed to make sure that the circuit was in the correct place and orientation.

6.2 Magnetic Circuit with Low Current in Field Free Space

The experiment with low current was conducted in the laboratory as the preliminary test of the magnetic circuit. A current of 13 Amps was chosen for this purpose. Figure 6.1 below shows the simulation results for current between 0 to 15 Amps. From the graph below we can predict the magnetic field at the center of the gap. The magnetic field should be approximately 0.06 T for 13 Amps drive.

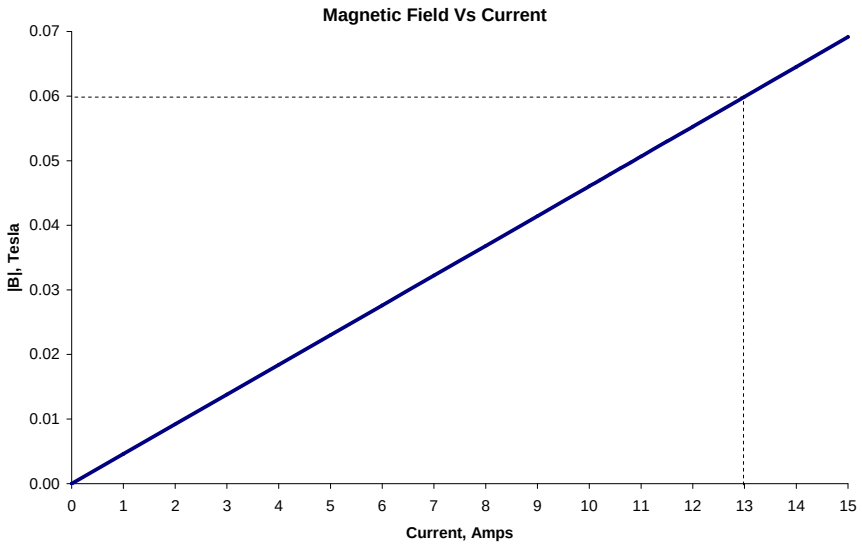

Figure 6.1: Magnetic field magnitude for current range from 0 to 15 Amps.

The data of this experiment were collected in the horizontal and vertical location of the gap of the magnetic core as illustrated in Figure 6.2.

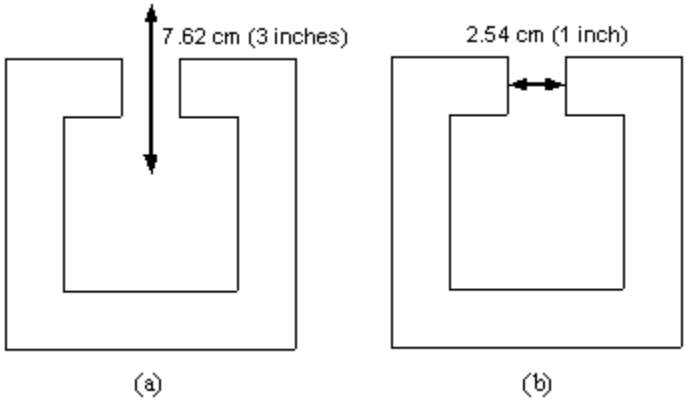

Figure 6.2: The location and orientation of data collected for low current experiment (a) vertical data (b) horizontal data

The data on the vertical location of the magnetic core were taken evenly below and above the center of the gap for a total length of 7.62 cm (3 inches). While for the horizontal location, the data were taken only in the gap of the magnetic core for a total length of 2.54 cm (1 inch). The data were then compared with the simulation results from FEMM as shown in Figure 6.3 and 6.4 below. Figure 6.3 compares the data in the vertical location for the simulation and the actual performance of the magnetic circuit. Figure 6.4 compares the data for the horizontal reading.

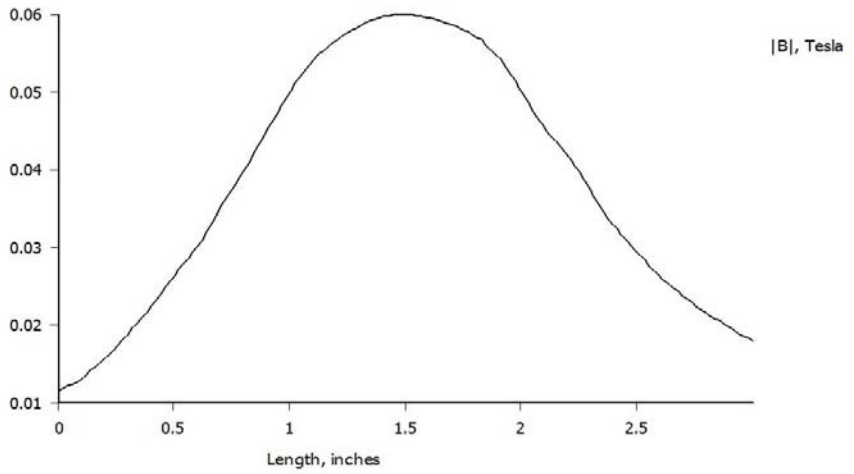

(a)

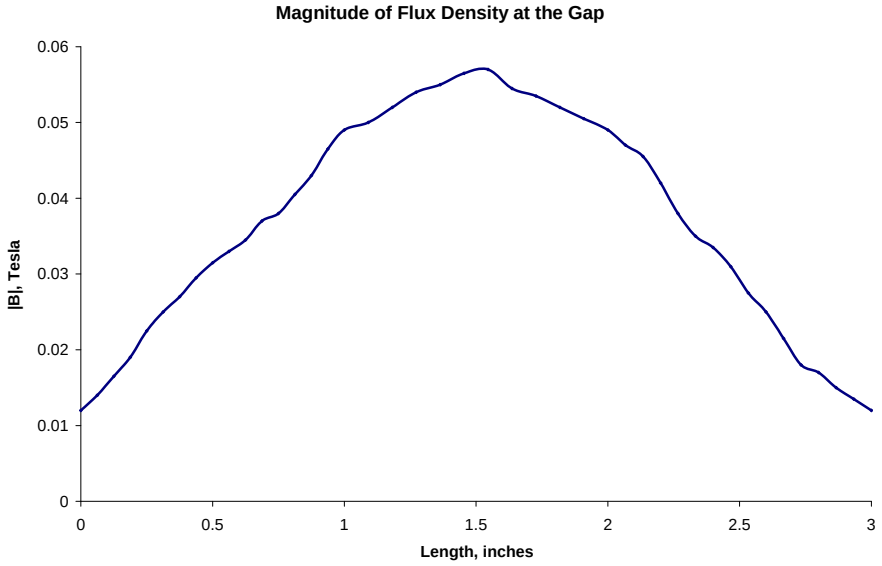

(b)

Figure 6.3: Magnitude of the flux density, |B| at the gap in the vertical direction (a) Simulation result from FEMM (b) Experimental result

From Figure 6.3, we can see that the data have the same pattern and the maximum data for simulation and experimental data are very close. The length between 1 and 2 inches is the length inside the gap. We can see that the maximum is at the center point of the gap.

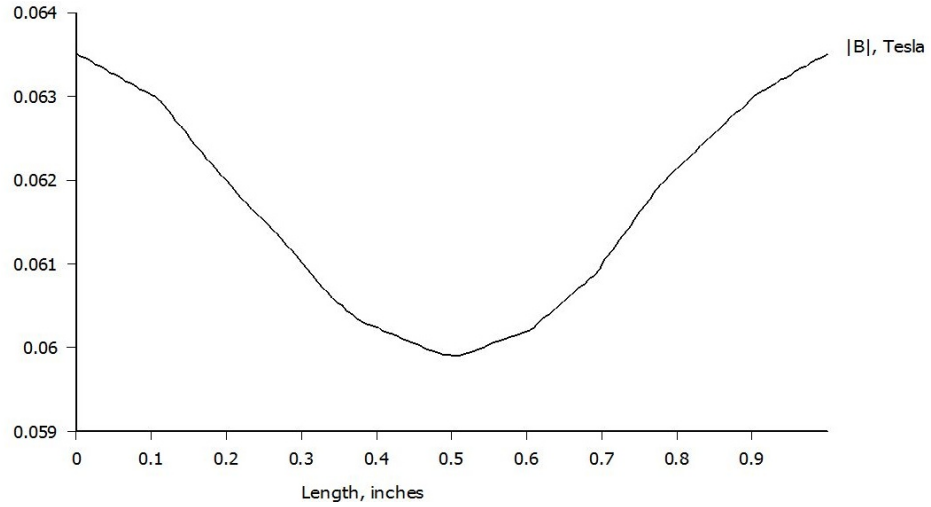

(a)

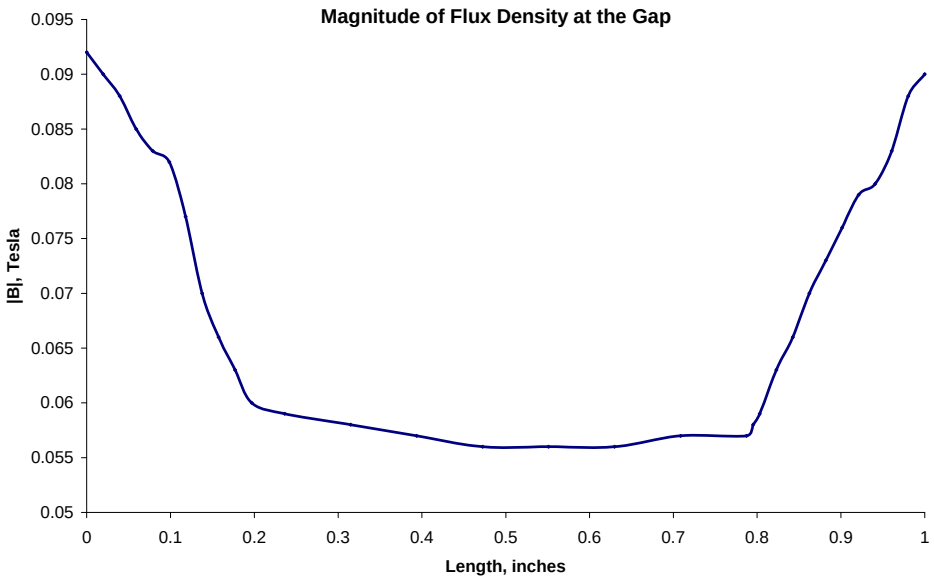

(b)

Figure 6.4: Magnitude of the flux density, |B| at the gap in the horizontal direction

(a) Simulation result from FEMM (b) Experimental result

From Figure 6.4, we can see that the pattern of the experimental data is not exactly the same as simulation but the minimum point of the data is almost the same as the simulation result. This minimum point is located at the center of the gap and has an

accuracy of 97% when compared to the simulation data. The difference at the start and end of the graph is largely due to the way data were taken when we conducted the measurement. The magnetic probe cannot easily and accurately measure the field near the core due to fringing effects from the core and, furthermore, the probe has to be held properly by hand. When the magnetic probe is very close and touches the magnetic core, it will give a higher magnetic field reading than true. From Figure 6.3 and 6.4 above, we also can see that the data are not as smooth as the simulation data due to this effect.

Based on the data taken for the low current measurement, we can conclude that the magnetic circuit is giving us a magnetic field that similar to that predicted in simulation. We then proceeded to the high current measurement which is the actual current used in the cyclotron facility to deflect the beam.

6.3 Magnetic Circuit with High Current in Field Free Space

The experiment using high currents in the laboratory was conducted with several currents. Since we applied high current to the magnetic circuit, we didn't use series resistors to control the current. Instead we added more parallel wire to the magnetic circuit. This is because we needed only very low resistances. Since the wire itself had its own resistance, we only used the length of wire as a resistance to control the current applied to the coil.

The main purpose of this test is to measure the real performance of the circuit before applied to the cyclotron facility. Three levels of current were measured for this

purpose; 114 Amps, 80 Amps and 55 Amps. Figure 6.5 below shows the predicted results from these currents.

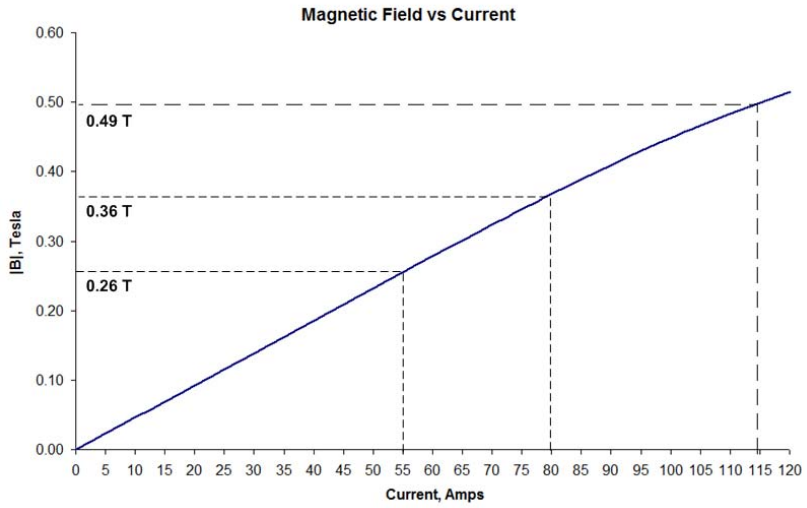

Figure 6.5: The simulation result of 114 Amps, 80 Amps and 58 Amps currents when applied to the magnetic circuit.

As seen from Figure 6.5 above, the magnetic field of 114 Amps, 80 Amps and 55 Amps are 0.49 T, 0.36 T and 0.26 T respectively. The results from measurement at the laboratory are shown in Table 6.1 below:

Table 6.1: The result of measurement using magnetic probe at the center of the gap

Current (Amps)	Magnetic Field (Tesla)
114	0.305
80	0.224
55	0.175

From the table above, we can conclude that the results are approximately 60% to 70% of the simulation result. The difference is largely due to the heat generated from the coils, flux leakage, fringing effects and probably gaps in the winding of the coils. However, taking these results into consideration, this system was still considered acceptable to deflect the beam of the cyclotron.

6.4 Deflection of the Cyclotron Beam

The experiment to deflect the proton beams was conducted at the cyclotron facility at MURR. For this experiment, we used a diagnostic system to detect the deflection of the beam. The diagnostic system used a faraday cup to detect and measure the current from the beam to verify the position of the beam. For this thesis, we positioned the magnetic circuit as in Figure 4.12(b). The illustration of the magnetic circuit positioning in the cyclotron facility is shown in Figure 6.6 below. From this illustration, we can see that the force will be in the negative *x* position of the beam. In other word, the beam will be deflected to the left side.

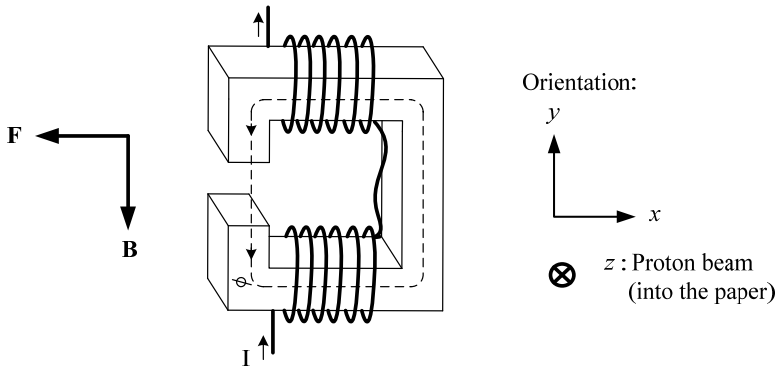

Figure 6.6: Positioning of the magnetic circuit at cyclotron facility

From the experiment as described in Section 6.3, we can conclude that the magnetic circuit performed at an average 65% of the predicted magnitude. The magnetic coil was placed on the beam drift tube and three values of current were supplied to it. The approximate magnetic field produced for these three currents is shown in Table 6.2 below.

Table 6.2: The approximation of magnetic field produced with 65% efficiency

Current (Amps)	Magnetic Field (Tesla)
55	0.175
50	0.150
42	0.130

Figure 6.7 below shows the predicted deflection of the beam in a 60.96 cm (24 inches) drift tube when the magnetic field given is produced from the magnetic circuit. The deflections are 0.46 cm, 0.40 cm and 0.34 cm for 55 Amps, 50 Amps and 42 Amps respectively.

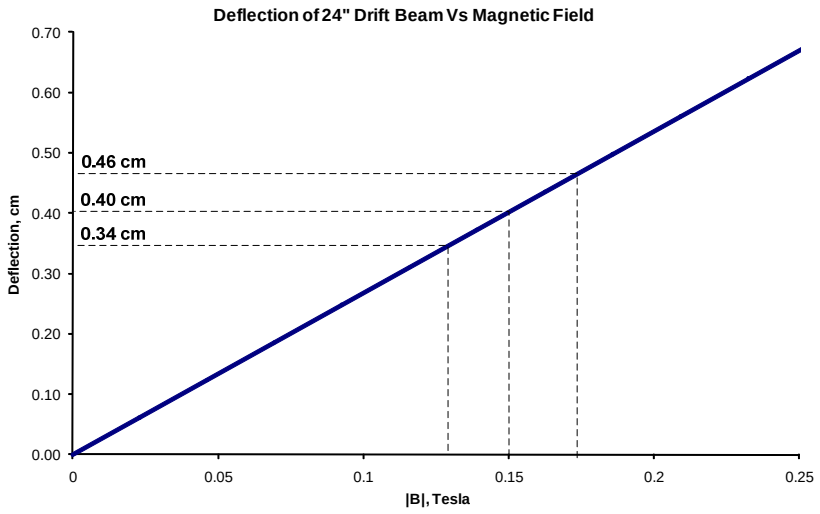

Figure 6.7: The predicted deflection of the beam in a 60.96 cm (24 inches) drift tube when given the magnetic field data from Table 6.2

As explained in Chapter 4, Section 4.6, two methods were used to verify the results from the experiment. One used a witness plate where we can physically see the beam location and make a measurement of deflection. The other method used a Faraday cup.

The results from the witness plates are shown as follows:

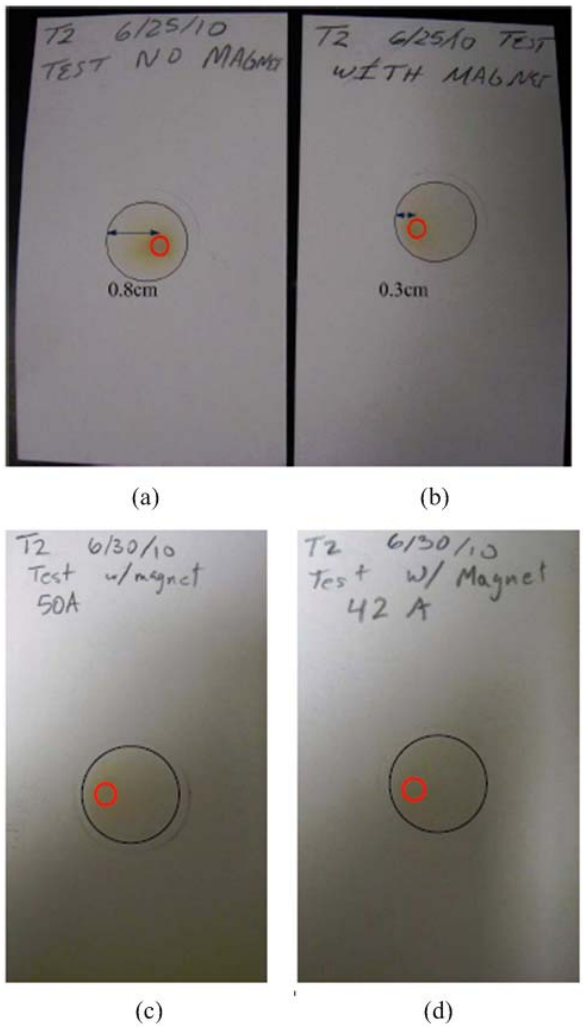

Figure 6.8: The results from witness plates (beam pattern outline enhanced to make clear in this reproduction)

Figure 6.8 (a) shows the beam position in a normal condition without the influence of the magnetic circuit. The beam position is almost at the center, but slightly to the right side. The distance from the left edge of the beam drift tube was approximately 0.8 cm. In the first experiment 55 Amps were applied to the coil and as we can see from

Figure 6.8 (b), the beam was moved to the left. The measurement taken from the left edge of the beam tube was roughly 0.3 cm. This showed that the beam was deflected by approximately 0.5 cm. Figure 6.8 (c) and (d) show the beam deflection at 50 Amps and 42 Amps. The beam was still to the left, again with a deflection of roughly 0.5 cm. This is consistent with prediction as we can see from Figure 6.7. Comparing theoretical to actual deflection, the difference is only approximately 0.06 cm in each case.

The other method to show the deflection is by taking currents measurement from a Faraday cup. The first step used a full exposure measurement to the Faraday cup set-up as shown previously in Figure 4.13 (a). The reading from this set-up was 5 μA. After that a partial exposure measurement was taken. The Faraday cup was placed in a right and left position as shown in Figure 4.15 (b) and (c) respectively. Table 6.3 below shows the results from the Faraday cup readings in these positions.

Table 6.3: Faraday cup reading

Magnetic field value	**Faraday cup reading** (μA)	
	Left	**Right**
0 T	1	2
0.175 T	1	0
0.150 T	1	0
0.137 T	1	0

From Table 6.3 above, we can see that when there was no magnetic field applied to the proton beam, the Faraday cup gave a higher reading at the right position of the

target. As we can see from the witness plate experiment above, the beam starts out slightly to the right side of the tube. The current to the Faraday cup is lower because the size of the aluminum plate being exposed to the proton beam is relatively small compared to full exposure. When we drive the magnetic coil giving 0.175 T, 0.15 T and 0.13 T as described in Table 6.2, the reading from the Faraday cup showed no current on the right side and only current on the left side of the tube. The beam had moved to the left as predicted.

CHAPTER 7

CONCLUSIONS AND FUTURE WORKS

7.1 Conclusions

The topics discussed in this thesis have focused on the development of a control system to deflect a cyclotron proton beam. The control system is very important to optimize the beam's function. The cyclotron facility at MURR is a biomedical cyclotron which is used for PET applications. The optimization of the beam will directly affect radioisotope production. The main goal of this thesis was to develop a system that can control the proton beam and characterized it by a diagnostic system.

The control system was successfully developed. A magnetic circuit was used as a main instrument to deflect the beam. The force correlated with the magnetic field deflected a moving charged particle. The currents driving the magnetic circuit were used to increase or decrease the distant of deflection since the changing currents is proportional to the changing magnetic field produced from the magnetic circuit. Users can change the direction of the deflection by changing the position of the magnetic coil or

current orientation. A diagnostic system was used to measure and characterized the proton beam deflections.

To predict the performance of the control system being developed, analysis using finite element methods was conducted. Simulations of different current distributions in the magnetic circuit were performed. The simulations predicted performance of the control system. From experiment, it was shown that the magnetic coil provided approximately 65% of the actual predicted magnetic field. Many factors contribute to this reduced performance such as the heat generated from the coils, flux leakage and gaps at the winding of the coils, which was very difficult to overcome in a practical experiment.

This thesis demonstrated the results obtained from an experiment on the cyclotron facility. We successfully deflected the beam as we predicted from the calculations and simulations. The witness plates and Faraday cup enable us to measure the beam's deflections with the change of current from the current supply.

7.2 Future Work

This research will encourage more work in the improvement of both the beam's control and in the target performance since these two are correlated with each other. The continuous improvement and optimization of the proton beam will attract more researchers. The work done in this thesis will be a jump start for a more complicated and sophisticated enhancement of the beam's functionality. Beams that can transport charged particles for a longer distant can also be developed. In this thesis, the mechanism to steer

proton beams was constructed. Focusing components using quadrupole magnet systems can be developed in future work.

This thesis also opens research in the study of the cyclotron target. Every target has its own unique radioisotope yield. This work opens the possibility of studying the effect of varying the bombardment distribution of the target to affect its gain. More study need to be conducted in the future on the precise bombardment of the targets.

REFERENCE

[1] T. J. Ruth, "Radionuclide production for the biosciences," in *Particle Accelerator Conference, 1995., Proceedings of the 1995*, 1995, pp. 67-69 vol.1.

[2] D. E. Kang, *et al.*, "Clinical Use of Fluorodeoxyglucose F 18 Positron Emission Tomography for Detection of Renal Cell Carcinoma," *The Journal of Urology,* vol. 171, pp. 1806-1809, 2004.

[3] D. W. McCarthy, *et al.*, "Efficient production of high specific activity 64Cu using a biomedical cyclotron," *Nuclear Medicine and Biology,* vol. 24, pp. 35-43, 1997.

[4] A. Obata, *et al.*, "Production of therapeutic quantities of 64Cu using a 12 MeV cyclotron," *Nuclear Medicine and Biology,* vol. 30, pp. 535-539, 2003.

[5] V. S. Le, *et al.*, "Alternative method for 64Cu radioisotope production," *Applied Radiation and Isotopes,* vol. 67, pp. 1324-1331.

[6] S. Humphries, *Charged particle beams*. New York: Wiley, 1990.

[7] M. P. Dehnel, *et al.*, "The design and operation of an industrial beam transport system for 15-30 MeV protons," in *Industry Applications Society Annual Meeting, 1991., Conference Record of the 1991 IEEE*, 1991, pp. 1374-1380 vol.2.

[8] M. P. Dehnel, *et al.*, "A compact cost-effective beamline for a PET Cyclotron," *Nuclear Instruments and Methods in Physics Research Section B: Beam Interactions with Materials and Atoms,* vol. 261, pp. 809-812, 2007.

[9] M. P. Dehnel, *et al.*, "Industrial Beamline Design for Radioisotope Production," *CYC2004, Tokyo,* p. 486, 2004.

[10] M. P. Dehnel, *et al.*, "Beamline developments in commercial cyclotron facilities," *Nuclear Instruments and Methods in Physics Research Section B: Beam Interactions with Materials and Atoms,* vol. 241, pp. 655-659, 2005.

[11] J. E. Theroux, *et al.*, "A 'short port' beamline for mounting custom targets to a GE PETtrace cyclotron," *Cyclotron and Their Applications, Eighteenth International Conference,* pp. 361-363, 2007.

[12] S. Wei, *et al.*, "Beam line design for a 100 MeV high intensity proton cyclotron at CIAE," *Nuclear Instruments and Methods in Physics Research Section B: Beam Interactions with Materials and Atoms,* vol. 261, pp. 65-69, 2007.

[13] M. Oothoudt, *et al.*, *Automatic beam position control at Los Alamos Spallation Radiation Effects Facility (LASREF)*, 1997.

[14] J. Sherman, *et al.*, *Status report on a dc 130-mA, 75-keV proton injector*, 1997.

[15] J. Sherman, *et al.*, *Development and test results of the low-energy demonstration accelerator (LEDA) proton injector on a 1.25 MeV cw radio frequency quadrupole*, 1998.

[16] L. D. Hansborough, *et al.*, *Mechanical engineering of a 75-keV proton injector for the Low Energy Demonstration Accelerator*, 1997.

[17] M. H. Phillips and et al., "Effects of respiratory motion on dose uniformity with a charged particle scanning method," *Physics in Medicine and Biology,* vol. 37, p. 223, 1992.

[18] V. P. Derenchuk, "A continuous wave microwave proton source and low energy beam transport for the IUCF cyclotrons," *Review of Scientific Instruments,* vol. 75, pp. 1851-1853, 2004.

[19] M. Chiari, *et al.*, "Measurement of low currents in an external beam set-up," *Nuclear Instruments and Methods in Physics Research Section B: Beam Interactions with Materials and Atoms,* vol. 188, pp. 162-165, 2002.

[20] P. Limão Vieira and R. F. M. Lobo, "Low energy electron beam for time-of-flight ionization measurements," *Vacuum,* vol. 52, pp. 19-22, 1999.

[21] K. L. Brown and G. W. Tautfest, "Faraday-cup monitors for high-energy electron beams," *The Review of Scientific Instruments,* vol. 27, pp. 696-702, 1956.

[22] V. Auzelyte, *et al.*, "On-line measurement of proton beam current in pA range," *Nuclear Instruments and Methods in Physics Research Section B: Beam Interactions with Materials and Atoms,* vol. 249, pp. 760-763, 2006.

[23] J. A. Cobble, *et al.*, "High resolution laser-driven proton radiography," *Journal of Applied Physics,* vol. 92, pp. 1775-1779, 2002.

[24] J. Shaw, *et al.*, "A high power Faraday cup to measure extracted beam current from the Bates South Hall Ring," in *Particle Accelerator Conference, 1997. Proceedings of the 1997*, 1997, pp. 2274-2275 vol.2.

[25] H.-C. Tay and G. W. Swift, "Magnetic Field Behavior of a Deeply Saturated Soft-Iron Core with a Concentrated Winding," *Power Delivery, IEEE Transactions on,* vol. 1, pp. 243-249, 1986.

[26] Y. B. Tang, *et al.*, "Design of a permanent magnetic circuit with air gap in a magnetic refrigerator," *Magnetics, IEEE Transactions on,* vol. 40, pp. 1597-1600, 2004.

[27] S. Moreau and J.-C. Trigeassou, "Modelling and identification of a non-linear saturated magnetic circuit: Theoretical study and experimental results," *Mathematics and Computers in Simulation,* vol. 71, pp. 446-459, 2006.

[28] S. C. Bell and P. S. Bodger, "Power transformer design using magnetic circuit theory and finite element analysis — A comparison of techniques," in *Power Engineering Conference, 2007. AUPEC 2007. Australasian Universities*, 2007, pp. 1-6.

[29] E. C. Shaffer, *et al.*, "Magnetostatic analysis using a general purpose finite element program," in *System Theory, 1995., Proceedings of the Twenty-Seventh Southeastern Symposium on*, 1995, pp. 330-334.

[30] A. Kenny, *et al.*, "An integrated magnetic circuit model and finite element model approach to magnetic bearing design," in *Energy Conversion Engineering Conference, 2002. IECEC '02. 2002 37th Intersociety*, 2002, pp. 181-184.

[31] D. Meeker, "FEMM," <*http://www.femm.info/wiki/HomePage*>, 2006.

[32] D. Vasic, *et al.*, "Pulsed eddy-current nondestructive testing of ferromagnetic tubes," *Instrumentation and Measurement, IEEE Transactions on,* vol. 53, pp. 1289-1294, 2004.

[33] J. Bohlmark, *et al.*, "Guiding the deposition flux in an ionized magnetron discharge," *Thin Solid Films,* vol. 515, pp. 1928-1931, 2006.

[34] S. A. Mazlan, *et al.*, "Magnetic circuit design for the squeeze mode experiments on magnetorheological fluids," *Materials & Design,* vol. 30, pp. 1985-1993, 2009.

[35] C. Qiushi and A. Konrad, "A review of finite element open boundary techniques for static and quasi-static electromagnetic field problems," *Magnetics, IEEE Transactions on,* vol. 33, pp. 663-676, 1997.

[36] E. O. Lawrence, "Method and apparatus for the acceleration of ions," U.S Patent 1948384, 1934.

[37] GE_Healthcare, "PETtrace SITE PLANNING GUIDE," pp. 81-84, 2007.

[38] N. N. Rao, *Basic electromagnetics with applications*. Englewood Cliffs, New Jersey: Prentice-Hall, Inc, pp. 392-393, 1972.

[39] D. Brooks, "Fusing Current: When Traces Melt Without a Trace," *Printed Circuit Design, a Miller Freeman publication,* December,1998.

[40] D. Meeker, "Finite Element Method Magnetics, Version 4.2, User's Manual," February 2009.

[41] I. Stokes-Rees. Introduction to FEA with FEMM. *http://www.femm.info/wiki/Documentation/*.

APPENDIX

Magnetic Core Design 1:

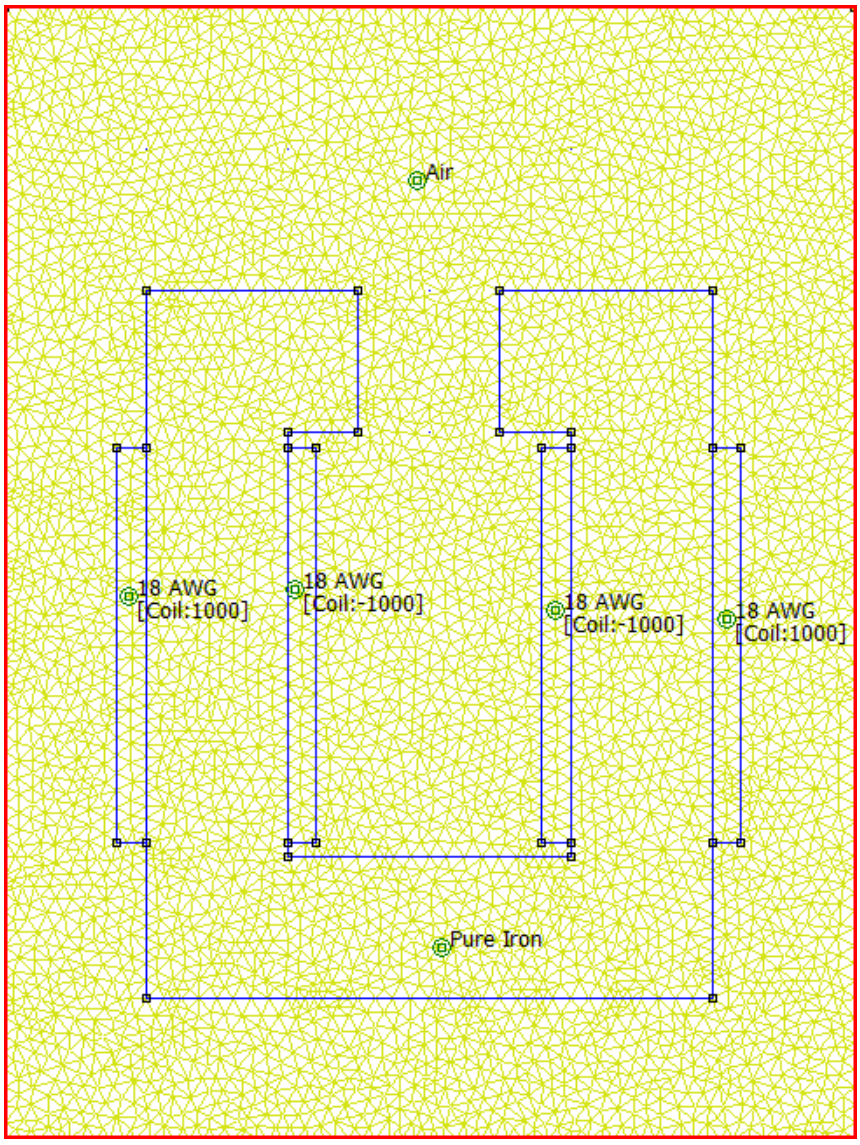

Figure 1: 2D cross section of core design

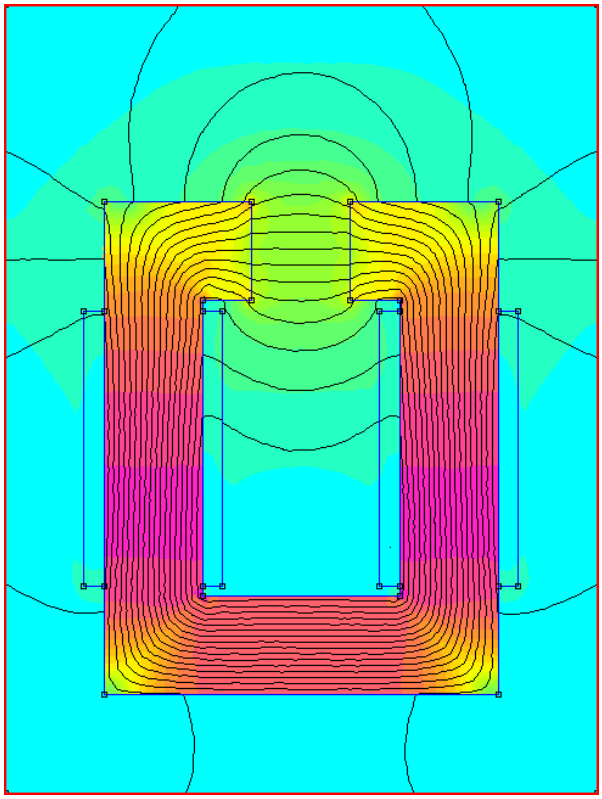

Figure 2: The result of analysis of core design

Magnetic core dimension: 4 inches x 5 inches

Coil circuit properties:

Table 1

18 AWG	20 AWG
Total current = 10 Amps	Total current = 10 Amps
Voltage Drop = 21.2719 Volts	Voltage Drop = 33.8229 Volts
Flux Linkage = 2.62301 Webers	Flux Linkage = 2.62306 Webers
Flux/Current = 0.262301 Henries	Flux/Current = 0.262306 Henries
Voltage/Current = 2.12719 Ohms	Voltage/Current = 3.38229 Ohms
Power = 212.719 Watts	Power = 338.229 Watts

Table 2

18 AWG	20 AWG
Total current = 100 Amps	Total current = 100 Amps
Voltage Drop = 212.719 Volts	Voltage Drop = 338.229 Volts
Flux Linkage = 4.45401 Webers	Flux Linkage = 4.65038 Webers
Flux/Current = 0.0445401 Henries	Flux/Current = 0.0465038 Henries
Voltage/Current = 2.12719 Ohms	Voltage/Current = 3.38229 Ohms
Power = 21271.9 Watts	Power = 33822.9 Watts

Result at the point at the center of the gap:

Coil current = 10 Amps	Coil current = 100 Amps
A = -0.0258576 Wb/m	A = -0.0446825 Wb/m
|B| = 0.673337 T	|B| = 1.17781 T
Bx = 0.673336 T	Bx = 1.17781 T
By = -0.000899975 T	By = -0.00143694 T
|H| = 535824 A/m	|H| = 937270 A/m
Hx = 535824 A/m	Hx = 937269 A/m
Hy = -716.177 A/m	Hy = -1143.48 A/m
mu_x= 1 (rel)	mu_x= 1 (rel)
mu_y = 1 (rel)	mu_y = 1 (rel)
E = 180395 J/m^3	E = 551962 J/m^3
J = 0 MA/m^2	J = 0 MA/m^2

Profile of magnetic density |B| along the gap based on Table 1 properties:

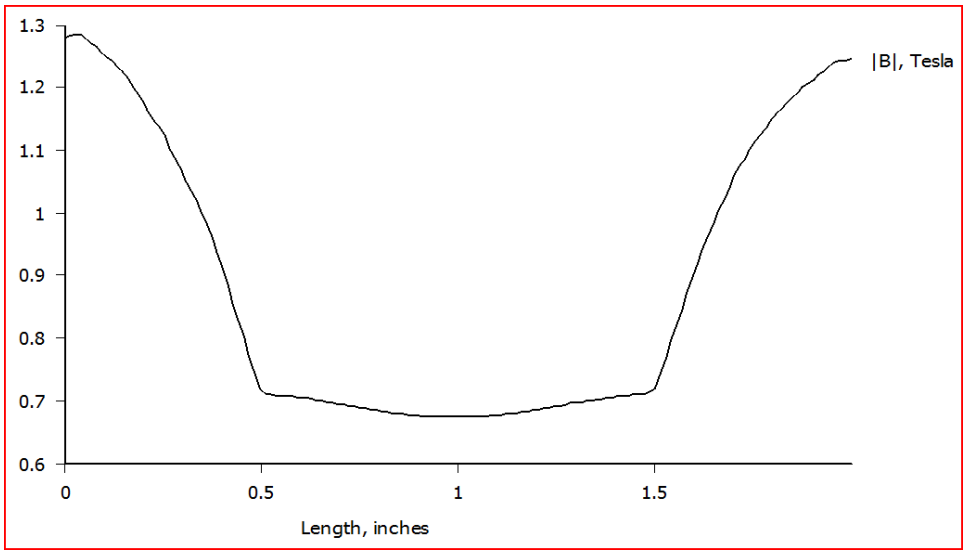

X-direction

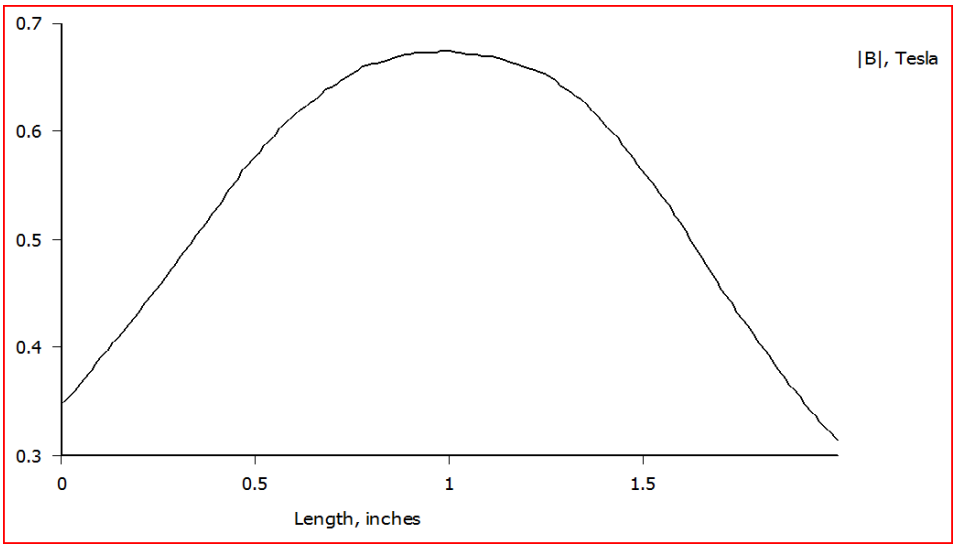

Y-direction

Profile of magnetic density |B| along the gap based on Table 2 properties:

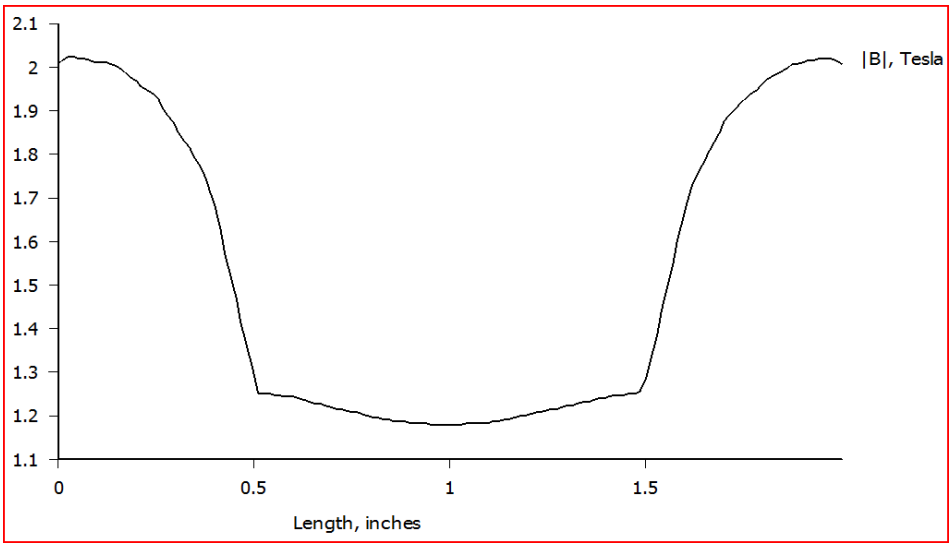

X-direction

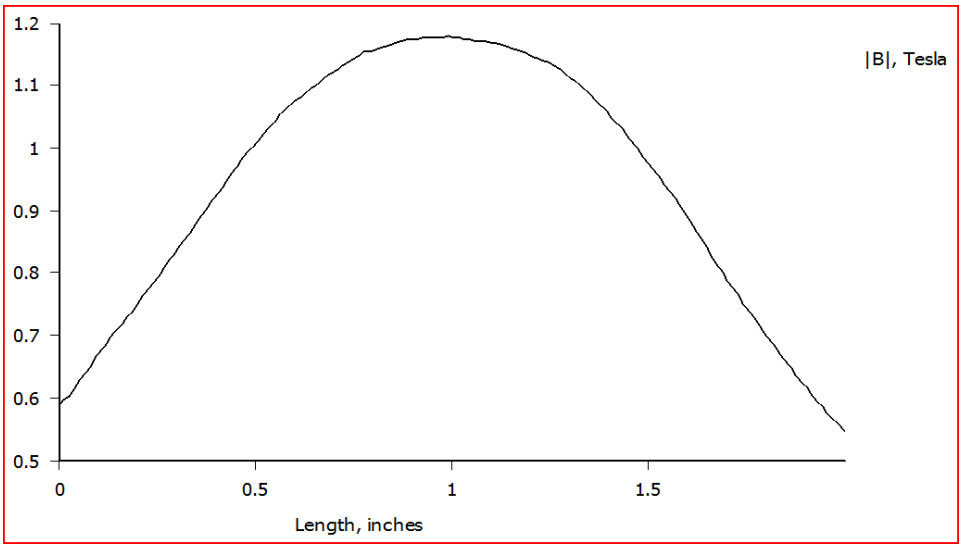

Y-direction

Magnetic Core Design 2:

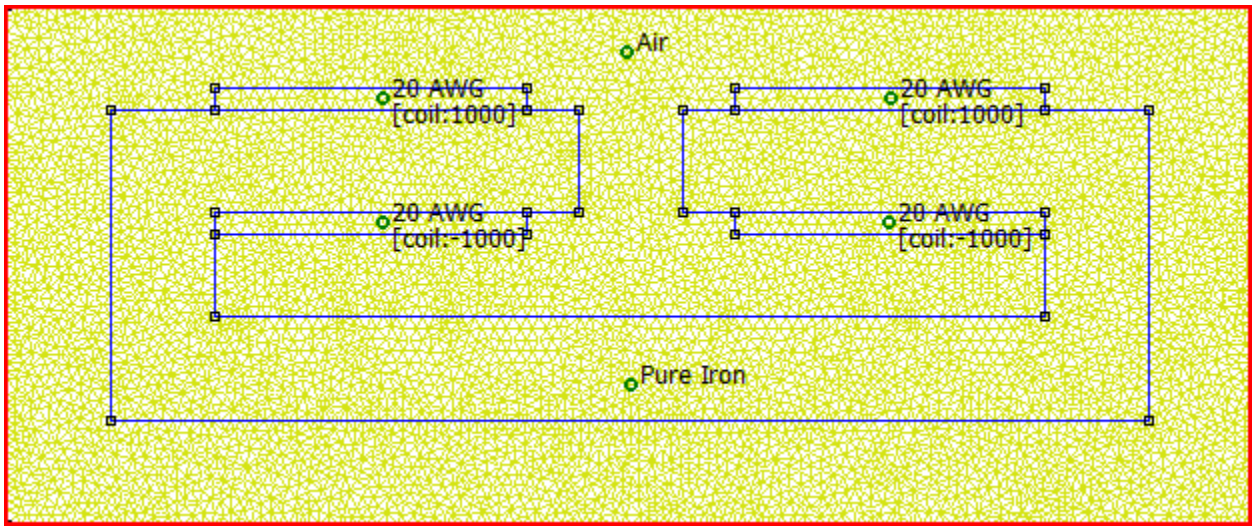

Figure 3: 2D cross section of core design

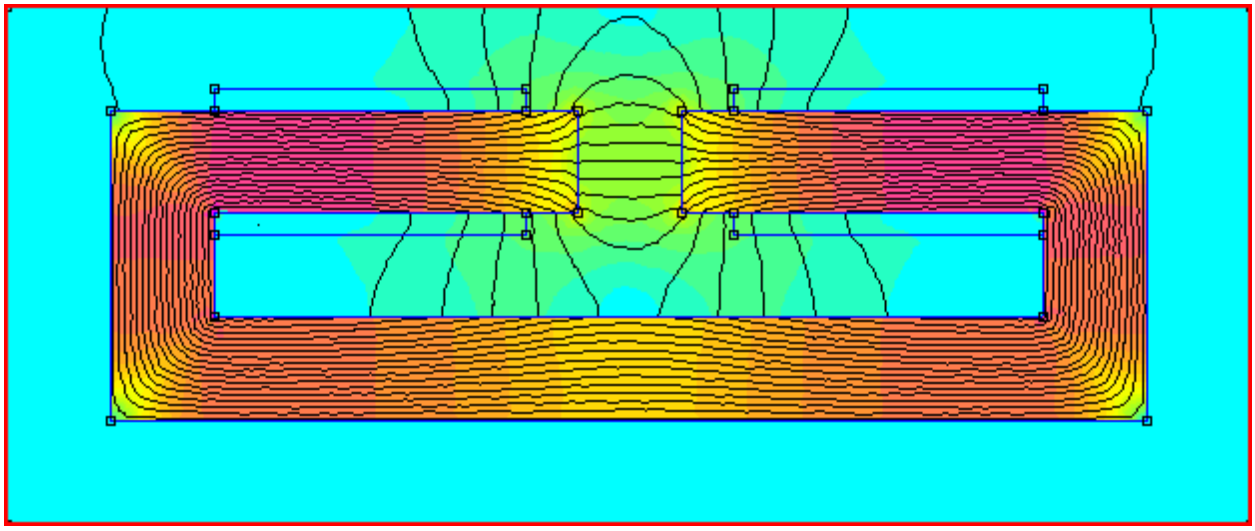

Figure 4: The result of analysis of core design

Magnetic core dimension: 10 inches x 5 inches

Coil circuit properties

Table 3

18 AWG	20 AWG
Total current = 10 Amps	Total current = 10 Amps
Voltage Drop = 21.2719 Volts	Voltage Drop = 33.8229 Volts
Flux Linkage = 2.51212 Webers	Flux Linkage = 2.51217 Webers
Flux/Current = 0.251212 Henries	Flux/Current = 0.251217 Henries
Voltage/Current = 2.12719 Ohms	Voltage/Current = 3.38229 Ohms
Power = 212.719 Watts	Power = 338.229 Watts

Table 4

18 AWG	20 AWG
Total current = 100 Amps	Total current = 100 Amps
Voltage Drop = 212.719 Volts	Voltage Drop = 338.229 Volts
Flux Linkage = 4.45401 Webers	Flux Linkage = 4.45448 Webers
Flux/Current = 0.0445401 Henries	Flux/Current = 0.0445448 Henries
Voltage/Current = 2.12719 Ohms	Voltage/Current = 3.38229 Ohms
Power = 21271.9 Watts	Power = 33822.9 Watts

Result at the point at the center of the gap:

Coil current = 10 Amps	Coil current = 100 Amps
A = -0.0211219 Wb/m	A = -0.0263174 Wb/m
|B| = 0.646348 T	|B| = 1.23152 T
Bx = 0.646347 T	Bx = 1.23152 T
By = -0.000567381 T	By = -0.00115963 T
|H| = 514347 A/m	|H| = 980010 A/m
Hx = 514347 A/m	Hx = 980010 A/m
Hy = -451.508 A/m	Hy = -922.8 A/m
mu_x= 1 (rel)	mu_x= 1 (rel)
mu_y = 1 (rel)	mu_y = 1 (rel)
E = 166224 J/m^3	E = 603450 J/m^3
J = 0 MA/m^2	J = 0 MA/m^2

Profile of magnetic density |B| along the gap based on Table 3 properties

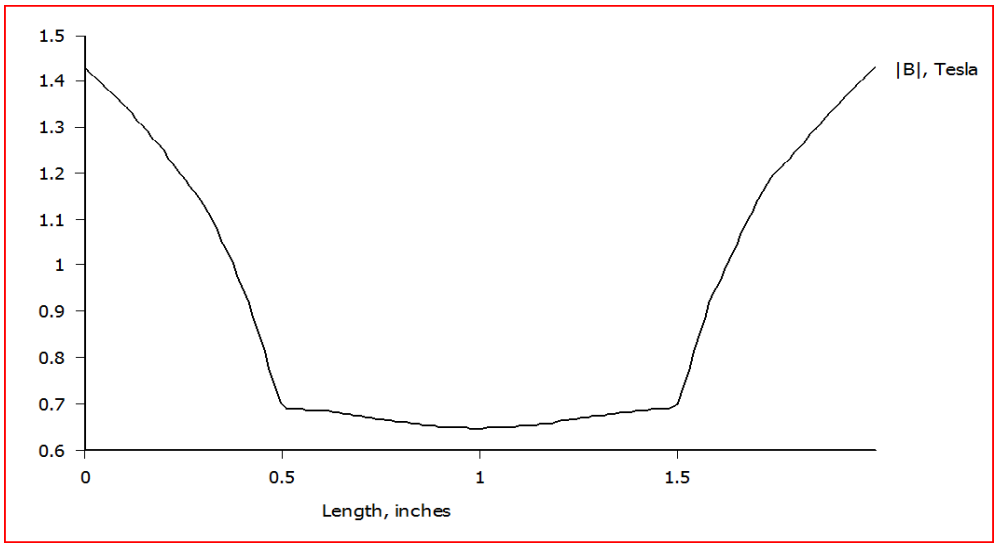

X-direction

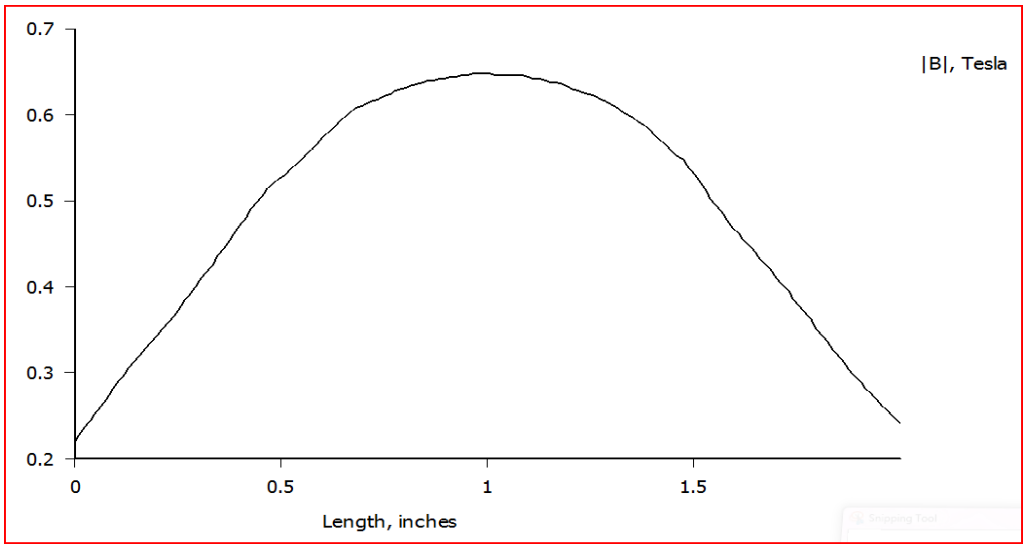

Y-direction

Profile of magnetic density |B| along the gap based on Table 4 properties

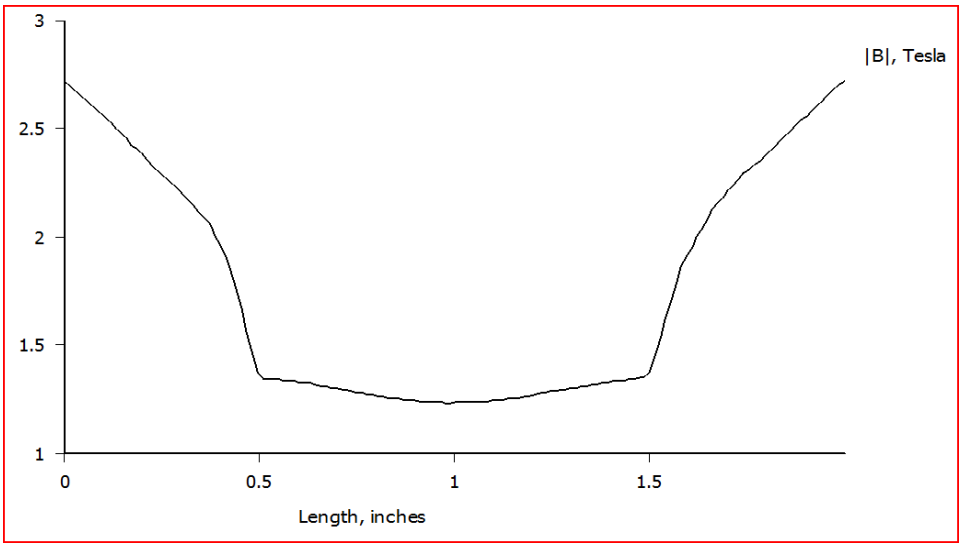

X-direction

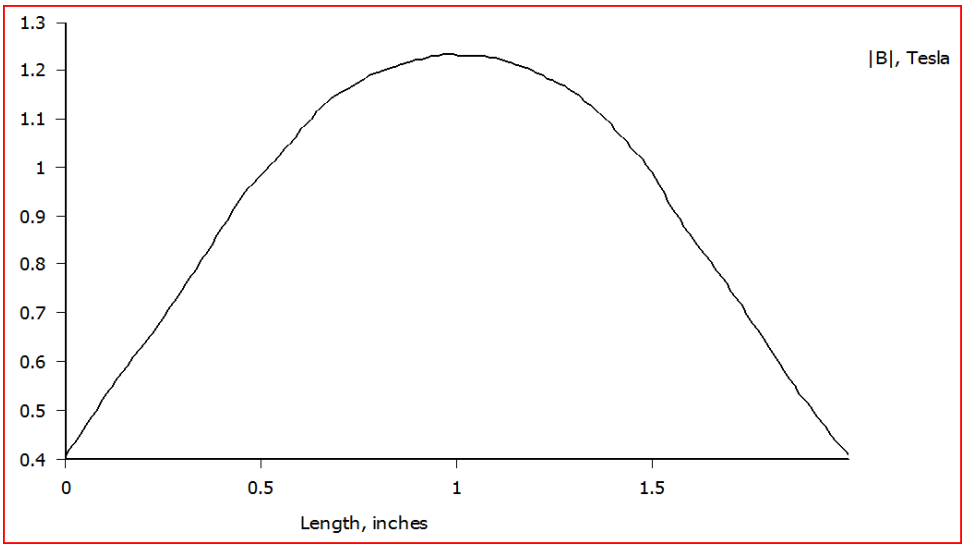

Y-direction